JGR Atmospheres

RESEARCH ARTICLE
10.1029/2022JD036815

Summer Dust Emissions From the Etosha Pan, Namibia: The Role of the Namib Anabatic-Sea Breeze System

Matthew Clements[1] and **Richard Washington**[1]

[1]Climate Research Lab, Oxford University Centre for the Environment, Oxford, UK

Key Points:

- An anabatic-sea breeze helps to drive austral summer dust emissions from one of the Southern Hemisphere's most prominent source areas
- The anabatic-sea breeze is present throughout the year, however is at its strongest, and propagates furthest inland during austral summer
- Variability in the strength of the system is driven by changes in the pattern of diabatic heating over the interior of southern Africa

Correspondence to:
M. Clements,
matthew.clements@ouce.ox.ac.uk

Citation:
Clements, M., & Washington, R. (2023). Summer dust emissions from the Etosha Pan, Namibia: The role of the Namib anabatic-sea breeze system. *Journal of Geophysical Research: Atmospheres*, *128*, e2022JD036815. https://doi.org/10.1029/2022JD036815

Received 22 MAR 2022
Accepted 5 FEB 2023

Abstract This paper utilizes Aerosol Index (AI) data from the Total Ozone Mapping Spectrometer (TOMS) instrument, along with ERA5 reanalysis data, to identify atmospheric processes contributing to the uplift of dust from the Etosha Pan through the annual cycle. Etosha is one of the most prominent source areas in the Southern Hemisphere, although very little is known about its meteorology outside of the peak dust season (August–October). Emissions in December (AI = 1.6) are shown to be comparable to those in September (AI = 1.7), the dustiest month in the TOMS record. Unlike in September however, when a nocturnal low-level jet is the primary emission mechanism, uplift in December is associated with an anabatic-sea breeze that develops along the Namib coast, and propagates inland to reach Etosha during the evening. The system is a response to the thermal contrast between the elevated interior plateau and the adjacent waters of the cool Benguela Upwelling System, and so is at its strongest during austral summer, when the area of maximum diabatic heating shifts south over southern Africa. Topographic channeling of the flow through the east-west orientated Hoanib River valley is shown to facilitate the inland propagation of the anabatic-sea breeze, and explains the persistence of the system at Etosha's latitude. Evening surface winds at Etosha, associated with the anabatic-sea breeze, are significantly stronger in the dustier December months, when diabatic heating over the subcontinent and hence the zonal thermal gradient are enhanced.

Plain Language Summary This paper uses satellite and meteorological data to identify the features of southern Africa's weather and climate that contribute to dust emission from the Etosha Pan throughout the year. Etosha is an important source of dust in the Southern Hemisphere, however very little work has been conducted there outside of the winter season, when emissions are at their highest. From the satellite data, it is shown that December is just as dusty as some of the winter months, however there is a difference in the low-level winds between the two seasons; in winter, emissions are driven by a morning peak in surface wind speeds, whereas emissions in December are driven by maximum surface winds during the evening. This evening peak in surface winds is shown to coincide with the arrival of a sea breeze at Etosha, with the system a response to the strong heating of the southern African plateau at this time of year. Evening surface winds associated with the sea breeze are stronger during the dustiest December months at Etosha, and are driven by enhanced heating over the subcontinent.

1. Introduction

Mineral aerosol (dust) has the ability to disturb atmospheric radiative transfer (Haywood & Boucher, 2000; Mahowald & Kiehl, 2003), fertilize marine and terrestrial ecosystems (Jickells et al., 2005; Koren et al., 2006; Mahowald et al., 2005; Wagener et al., 2008) and impact upon human health (Goudie, 2014; Middleton, 2017). For these reasons, dust constitutes an important component of the earth system, and so it is essential that it is accurately represented in state-of-the-art climate models (Boucher et al., 2013). In most coarse-resolution models, dust emission is parameterized, and is given as a function of the cube of surface wind speed u above a specified threshold u_t, so that;

$$q = (u - u_t)^3, when\, u > u_t \quad (1)$$

where q is the vertical sand flux (Knippertz & Todd, 2012; Kok et al., 2012). Realistic simulation of the emission process is therefore dependent on capturing the surface wind speed distribution in dust source areas, however evaluation studies show that models tend to miss the tail of low-frequency, high wind speed events that drive uplift (Evan, 2018; Roberts et al., 2017), an inevitable consequence of their inability to resolve some key atmospheric processes (Allen & Washington, 2014; Garcia-Carreras et al., 2013).

These key processes include the mix-down of momentum from nocturnal low-level jets (NLLJs) (Fiedler et al., 2013; Knippertz & Todd, 2012; Washington & Todd, 2005), downdrafts from convective storms (cold pool outflows) (Caton Harrison et al., 2021; Heinold et al., 2013; Marsham et al., 2013) and microscale dust devils or dry convective plumes (Jemmett-Smith et al., 2015; Knippertz & Todd, 2012). The current state of knowledge regarding these emission mechanisms comes largely from work conducted in a Saharan context, either through intensive observational campaigns (Washington et al., 2006), remote sensing (Schepanski et al., 2007, 2009) or modeling studies (Heinold et al., 2013; Todd et al., 2008). There are however other important dust source areas outside of North Africa (Prospero et al., 2002; Washington et al., 2003), and given the inability of models to capture salient features of the Saharan dust climatology (Evan et al., 2014; Roberts et al., 2017), it is necessary to investigate dust-emitting mechanisms, and test model fidelity in other geographical regions.

Remote sensing studies have identified a number of dust source areas across southern Africa (Prospero et al., 2002; Vickery et al., 2013), the most prominent of which is the Etosha Pan (Washington et al., 2003), located in northern Namibia. Whilst annual emissions are lower than those from the major North African sources (e.g., the Bodélé Depression), they are amongst the highest in the Southern Hemisphere, with comparable dust loadings to the Lake Eyre Basin in Australia (Washington et al., 2003). Whilst previous work has detailed some of the hydrological controls on the availability of sediment from the pan surface (Bryant, 2003; Mahowald et al., 2003), and developed detection algorithms of dust plumes from satellite derived data (Murray et al., 2016), very little attention has been given to the atmospheric processes contributing to the observed dust loadings. Observational data has shown a NLLJ to be a persistent feature of the boundary layer from August–October (Clements & Washington, 2021; Zunckel et al., 1996), with the mix-down of momentum during the morning breakdown of the jet identified as the primary emission mechanism during this season (Clements & Washington, 2021). It is not yet known however the extent to which the NLLJ sustains dust emissions beyond austral winter, or whether other atmospheric processes drive uplift at other points in the annual cycle.

Given the need to understand the atmospheric controls on dust emission, and subsequently refine the representation of relevant processes in numerical models, this paper aims to investigate the range of dust-emitting mechanisms operating throughout the annual cycle, in a relatively understudied yet regionally significant source area, by addressing the following key questions: (a) What is the annual cycle of dust emissions from the Etosha Pan? (b) How do the atmospheric processes responsible for driving dust emission from the Etosha Pan vary through the annual cycle? (c) What are the spatial and temporal characteristics of the dust emission mechanisms operating at the Etosha Pan, and what controls their variability? (d) How does variability in the processes described help to account for variability in austral summer dust emissions from the Etosha Pan? The remainder of the paper is structured as follows: Section 2 describes the location and climatic setting of the study area and details the data sources and methods employed. Results are presented in Sections 3–6, with each of the key questions addressed in turn. The results are discussed in Section 7 and the papers main findings are summarized.

2. Data and Methods

2.1. Physical Setting

The Etosha Pan is a flat salt pan situated in northern Namiba, covering an area of ≈4,800 km^2 (Prospero et al., 2002). It sits in a topographic depression, and drains a network of ephemeral channels (locally known as oshanas), with the catchment stretching north into the southern Angolan highlands (Preston-Whyte et al., 1994). Rainfall in the catchment and hence inundation of the pan is limited to October–April, when the area of tropical convection moves south. Stable, dry conditions preside over the subcontinent during austral winter, resulting from strong subsidence associated with the descending limb of the overturning Hadley circulation (Reason, 2017).

2.2. TOMS AI Data

Aerosol Index (AI) data from the Total Ozone Mapping Spectrometer (TOMS) instrument is used to monitor dust emissions from the Etosha Pan between 1980–1992 (key question a). During this time, the TOMS instrument was onboard the NASA Nimbus 7 polar-orbiting satellite and took measurements in six ultraviolet (UV) wavelengths, with the initial objective to track changes in the Earth's ozone (McPeters et al., 1996). However, given the absorbing properties of dust in UV wavelengths, the TOMS instrument has been used in numerous studies to identify major source areas (Prospero et al., 2002; Washington et al., 2003). The advantage UV remote sensing has over

visible and infrared (IR) wavelengths is its low reflectivity over land surfaces (including deserts), making for efficient detection of airborne dust particles (Torres et al., 2002). For a more detailed analysis of the TOMS instrument, see McPeters et al. (1996).

AI data is given in non-dimensional units, with absorbing aerosols returning positive values, and for dust, the magnitude of the AI signal reflects the optical depth of the aerosol (Bryant, 2003; Herman et al., 1997). The temporal frequency of the data is daily, and it has been projected onto a latitude-longitude grid of resolution 1.0° × 1.0°. In order to monitor dust emissions at Etosha, AI data from the central grid point (18.5°S, 15.625°E) of the plume is used. In Section 3, dust emissions at Makgadikgadi are also evaluated, with AI data also coming from the central grid point (20.5°S, 25.625°E) of the respective plume.

2.3. Reanalysis and Gridded Precipitation Data

ERA5 reanalysis data from the European Centre for Medium-Range Weather Forecasts (ECMWF) is used to identify the atmospheric processes contributing to dust emission at Etosha (key question b), and investigate their spatial and temporal characteristics, as well as the controls on their variability (key question c). ERA5 data covers the period 1950–present, with analysis fields output at hourly intervals, at a spatial resolution of ≈31 km, and 137 model levels in the vertical. Parameters extracted from the ERA5 data set for analysis include u and v components of wind (10 m and model level), temperature (2 m, model and pressure level), specific humidity (model level), top net thermal radiation and divergence (model level). Wind speed was calculated as the square root of the sum of the squared u and v components at each grid point ($ws = \sqrt{u^2 + v^2}$), outgoing longwave radiation (OLR) was calculated as the negative of top net thermal radiation, divided by the averaging period (3600 s), whilst potential temperature was calculated from the Poisson equation $\left(\theta = T(P_0/P)^k\right)$, where T is air temperature, P_0 is a reference pressure of 1,000 hPa, P is the atmospheric pressure and k is the Poisson constant. Where atmospheric data is presented for Etosha, the grid point closest to the centre of the pan (18.5°S, 15.625°E) is used.

The ERA5 data set benefits from over a decade of research and development since the release of the previous ECMWF reanalysis (ERA-Interim), with an increase in horizontal resolution, an improved data assimilation methodology and refined parameterization schemes (Hersbach et al., 2020). Upgrades to model parameterisations include the adoption of the "McRad" radiation scheme (Morcrette et al., 2008), improvements to the original precipitation and convective schemes (Bechtold et al., 2014), as well as advances in the treatment of subgrid turbulent mixing and orographic drag effects (Hersbach et al., 2020). ERA5 also features a new land surface scheme (HTESSEL), which, through the adoption of satellite derived vegetation datasets, has improved the representation of variables such as temperature and humidity at the surface (Boussetta et al., 2013; Hersbach et al., 2020). For a detailed discussion of the ERA5 reanalysis, including data assimilation systems, model setup, and an overview of performance, see Hersbach et al. (2020).

In Section 3, precipitation data from the Climate Hazards Group InfraRed Precipitation with Station data (CHIRPS) version 2.0 is used to investigate the effect of inundation on dust emissions at Etosha. CHIRPS utilizes satellite derived rainfall estimates in conjunction with station gauge data to produce a daily gridded precipitation data set from 1981 to near-present with a 0.05°, 0.05° horizontal resolution (Funk et al., 2015). In southern Africa, gauge data is provided by the Southern African Science Service Centre for Climate Change and Adaptive Land Management (SASSCAL) (Funk et al., 2015). For a full discussion of the CHIRPS data set, see Funk et al. (2015).

3. Annual Cycle of Dust Emissions at Etosha

The following sections address key question a: What is the annual cycle of dust emissions from the Etosha Pan?

3.1. Annual Cycle of Dust Emissions

Mean AI data from the TOMS instrument shows two major dust source areas in southern Africa (Figure 1); these are the Etosha and Makgadikgadi Pans, located in northern Namibia (18.75°S, 16.25°E) and north-eastern Botswana (20.75°S, 25.50°E) respectively. Previous studies have utilized TOMS data to demonstrate the predominance of these two source areas in their contribution to total southern African dust emissions (Prospero et al., 2002; Washington et al., 2003), with higher-resolution satellite data exposing more minor contributions from coastal Namib sources and the Kalahari (Murray et al., 2016; Vickery et al., 2013). The high (>1.5) mean AI values observed along the coast of Angola and northern Namibia from June to September (Figure 1) are not indicative of dust aerosol emissions, but are instead the result of savannah fires in the interior of the subcontinent

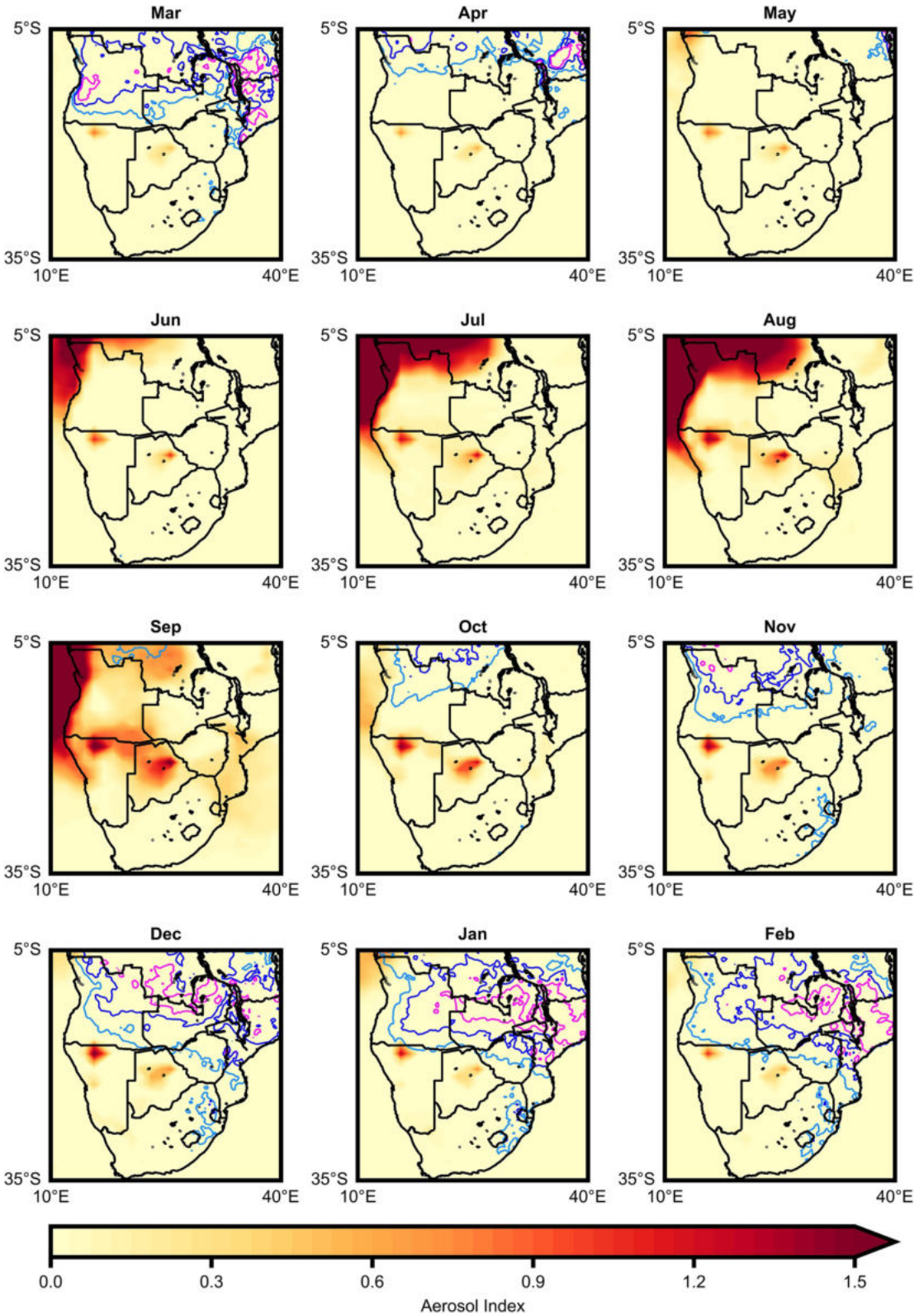

Figure 1. Mean Total Ozone Mapping Spectrometer AI data for 1980–1992. Mean precipitation data for 1981–1992 from the CHIRPS data set is plotted as 4 $mmday^{-1}$ (light blue), 6 $mmday^{-1}$ (blue) and 8 $mmday^{-1}$ (purple) contours.

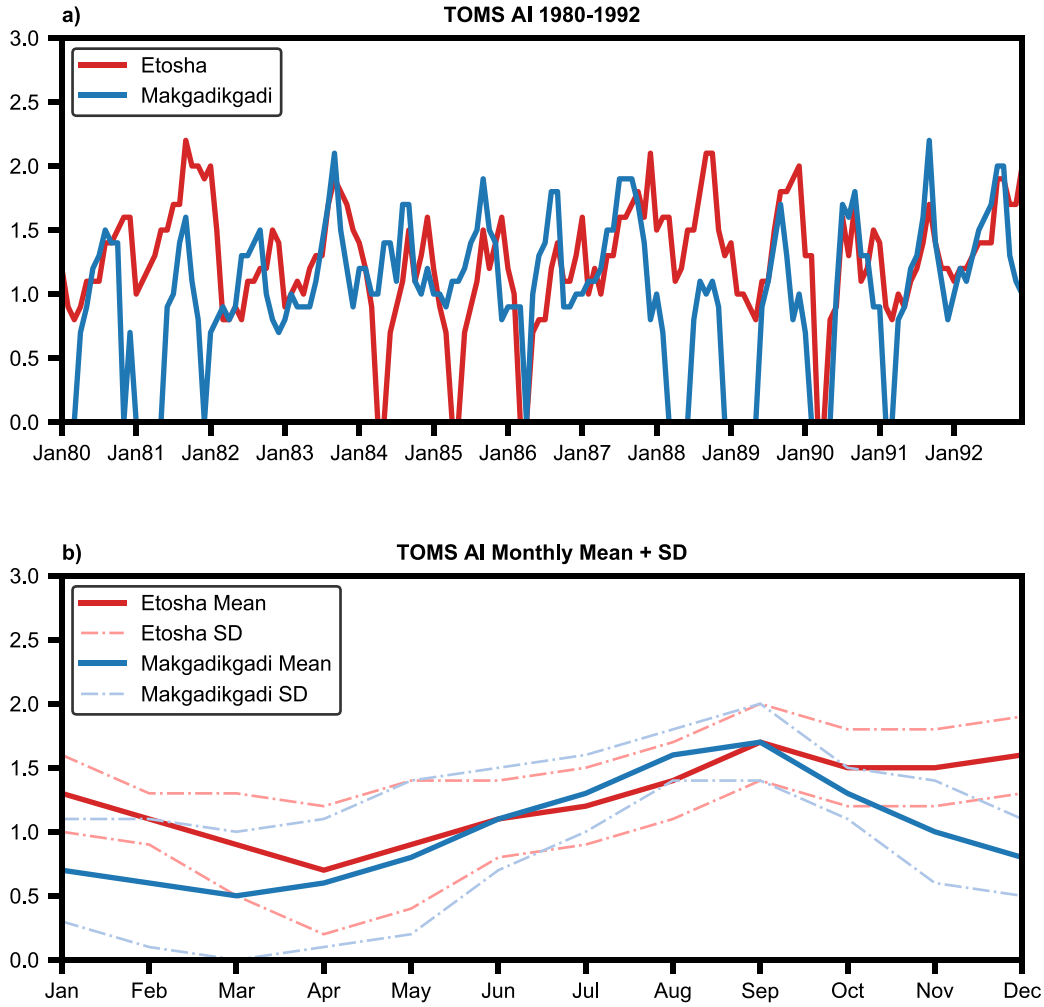

Figure 2. (a) Time series of AI data for the Etosha and Makgadikgadi pans, 1980–1992. (b) Monthly mean and standard deviation of AI for the Etosha and Makgadikgadi pans.

Table 1
Total Ozone Mapping Spectrometer AI Statistics 1980–1992

	Etosha		Makgadikgadi	
Month	AI Mean	AI SD	AI Mean	AI SD
January	1.3	0.3	0.7	0.4
February	1.1	0.2	0.6	0.5
March	0.9	0.4	0.5	0.5
April	0.7	0.5	0.6	0.5
May	0.9	0.5	0.8	0.6
June	1.1	0.3	1.1	0.4
July	1.2	0.3	1.3	0.3
August	1.4	0.3	1.6	0.2
September	1.7	0.3	1.7	0.3
October	1.5	0.3	1.3	0.2
November	1.5	0.3	1.0	0.4
December	1.6	0.3	0.8	0.3

(Herman et al., 1997; Sinha et al., 2003). The biomass burning aerosols are subsequently transported north-westward out over the Atlantic by the tropical easterlies which form part of the inflow toward the convective regions further north (Reason, 2017).

Figure 2a shows a time series of AI data for the Etosha Pan between 1980–1992, with monthly mean and standard deviation data plotted in Figure 2b and also summarized in Table 1. For reference, AI data for the Makgadikgadi Pan, southern Africa's other major dust source area, is also included. Dust emissions across the subcontinent increase through the winter months (Figure 2b), and peak at the end of the dry season (September), when the highest mean AI values are recorded at both Etosha (AI = 1.7) and Makgadikgadi (AI = 1.7) (Table 1), with a plume also stretching between the two source areas across the northern Kalahari (Figure 1). Mean AI values remain high (>1.5) at Etosha through spring and into summer; indeed, other than September, December (AI = 1.6) is the dustiest month in the TOMS record. This is in contrast to Makgadikgadi, where mean AI values fall to below 1.0 by December, and remain low (<1.0) through the rest of the summer months. Dust emissions across southern Africa reach a minimum from March to May, with mean AI values below 1.0 recorded for both major source areas.

Table 2
Etosha Total Ozone Mapping Spectrometer AI Statistics

	September		December	
Year	AI Mean	Days AI > 2	AI Mean	Days AI > 2
1980	1.4	2	1.6	7
1981	2.2	19	1.9	14
1982	1.2	0	1.4	4
1983	1.9	12	1.5	8
1984	1.5	2	1.6	10
1985	1.5	0	1.6	9
1986	1.4	2	1.3	4
1987	1.7	10	2.1	16
1988	2.1	19	1.3	3
1989	1.8	6	2.0	15
1990	1.7	2	1.5	6
1991	1.7	7	1.2	0
1992	1.9	13	2.0	18

3.2. Austral Summer Dust Emissions

The annual cycle of dust emissions at Etosha (and Makgadikgadi) described in Section 3.1 is closely linked to the annual cycle of wetting and drying across southern Africa, with fluvial input to the pan regulating the availability of erodible sediment (Bryant, 2003; Murray et al., 2016). Precipitation contours are shown on Figure 1, and reflect the southward migration of the tropical rainbelt during spring and summer, as well as the transition of the Angola Low from a dry to a moist convecting system (Howard & Washington, 2018; Munday & Washington, 2017; Reason, 2017). Shallow inundation events occur at Etosha during the wet season (October–April), and whilst initially suppressing dust emissions, they provide material that is readily deflated once dry (Bryant, 2003; Mahowald & Kiehl, 2003). Previous remote sensing studies have documented the resulting peak in dust emissions toward the end of the dry season (August–October) at Etosha (Prospero et al., 2002; Vickery et al., 2013; Washington et al., 2003), however very little attention has been given to summer dust emissions; this is despite the observation presented in Section 3.1 that mean AI values in December are the second highest for any month in the TOMS record.

Table 2 shows mean AI data for each December at Etosha between 1980–1992, with the number of individual days where values exceeded 2.0 also reported. The three dustiest December months (1987, 1989, 1992) and the three least dusty (1986, 1988, 1991) were used to construct composites of AI and precipitation (from the CHIRPS data set) (Figure 3). Precipitation composites for the preceding summer season (DJF-1) are also shown. Difference composites were calculated by subtracting the low AI composite from the high AI composite. As well as a more substantial plume at Etosha, greater AI values are observed across other parts of southern Africa in the high AI composite, with increased dust emissions at Makgadikgadi, across the southern Kalahari and along the Namib coast (Figure 3a). It is also drier in the Etosha catchment during the dusty December months, whereas elevated precipitation totals stretch into northern Namibia and southern Angola in the low AI composite (Figure 3b).

These findings, as well as the fact that the three dustiest December months at Etosha (1987, 1989, 1992) are immediately preceded by the three least dusty (1986, 1988, 1991) (Figure 2a, Table 2), suggest a strong hydrological influence on the availability of sediment during summer. A possible explanation is that increased precipitation in the Etosha catchment in the preceding DJF results in intermittent flow events and fluvial input into the pan. This at first suppresses dust emissions, but replenishes the supply of sediment, which is then deflated in the following year. Due to the increased wetting of the pan surface, the deposited sediment requires a prolonged period of drying before it can be entrained, hence shifting the timing of peak dust emissions from late winter to December. There is however very little difference in the preceding DJF precipitation between the high and low AI composites (Figure 3c), and so a far more likely explanation is that precipitation has an immediate impact in suppressing summer dust emissions, as is the case in the least dusty December months (Figure 3b). This reasoning is also corroborated by the coincidence of the dustiest December month (1987) with strong El Niño conditions; these events are associated with suppressed tropical convection over southern Africa, and hence reduced input to the Etosha pan. The decrease in AI values at Makgadikgadi through the spring and summer months owes to the location of the catchment area (further north and east), which results in earlier inflow to the pan, hence precluding dust emissions.

4. Atmospheric Controls on Dust Emissions at Etosha

The following sections address key question b: How do the atmospheric processes responsible for driving dust emission from the Etosha Pan vary through the annual cycle?

4.1. Nocturnal Low-Level Jet

Previous work at Etosha has focused on dust emissions at the end of the dry season, with the mix-down of momentum from a NLLJ identified as the primary emission mechanism (Clements & Washington, 2021). In

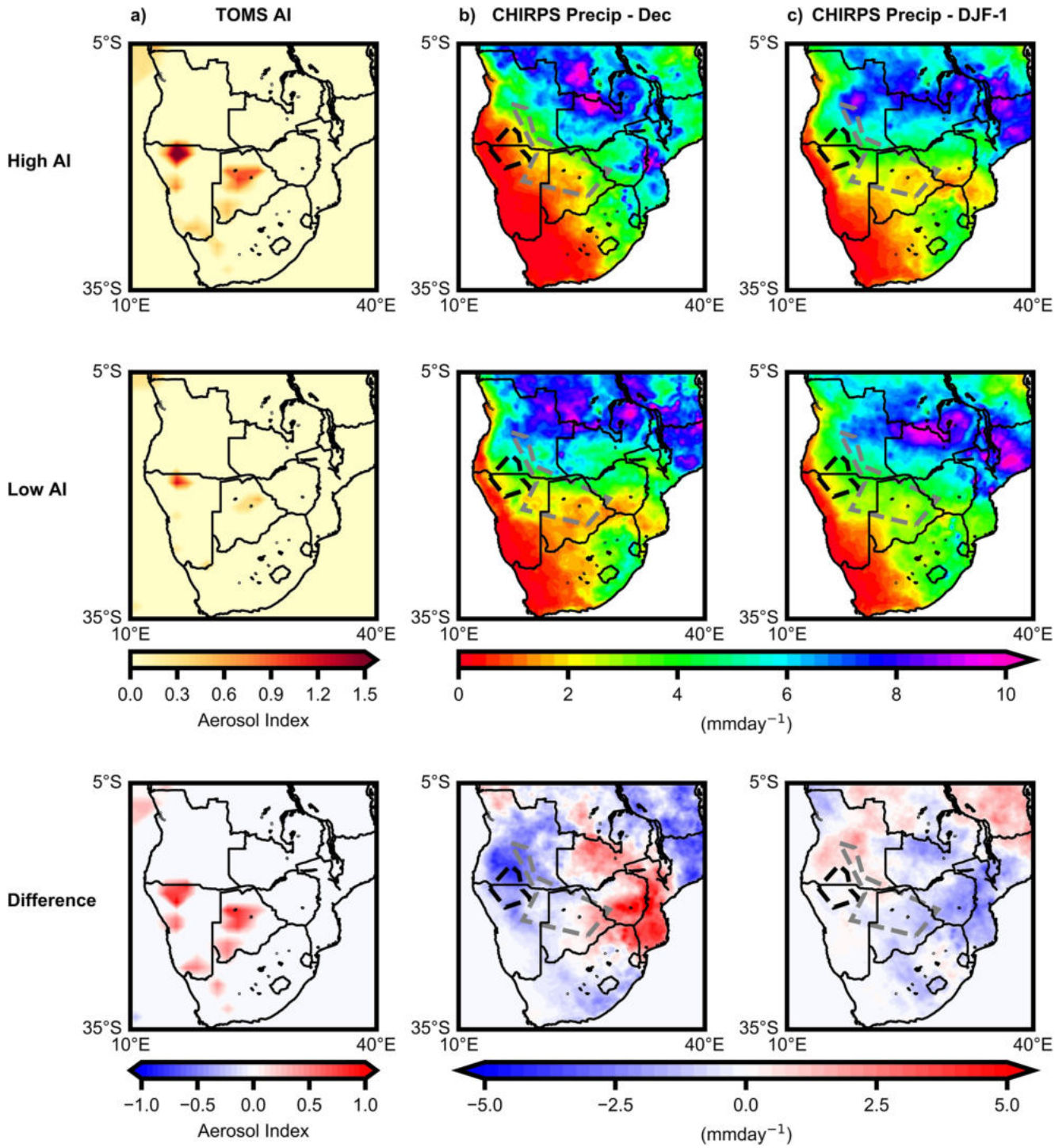

Figure 3. December high AI, low AI and difference composites of (a) AI, (b) December precipitation and (c) precipitation in the preceding DJF. The difference composites were calculated by subtracting the low AI from the high AI. In (b and c), the approximate location of Etosha's catchment is given by the black polygon and Makgadikgadi's by the gray.

order to investigate whether the NLLJ is a driver of summer dust emissions, composite wind speed-height profiles have been constructed using ERA5 data for the three dustiest December months in the TOMS record (1987, 1989, 1992) (Figure 4a); for reference, profiles for the three dustiest September months (1981, 1988, 1983) (Table 2) are also shown. September was chosen as it is the dustiest month in the TOMS record, and in situ observational data has shown the NLLJ to be a persistent feature of the nocturnal boundary layer during the month (Clements

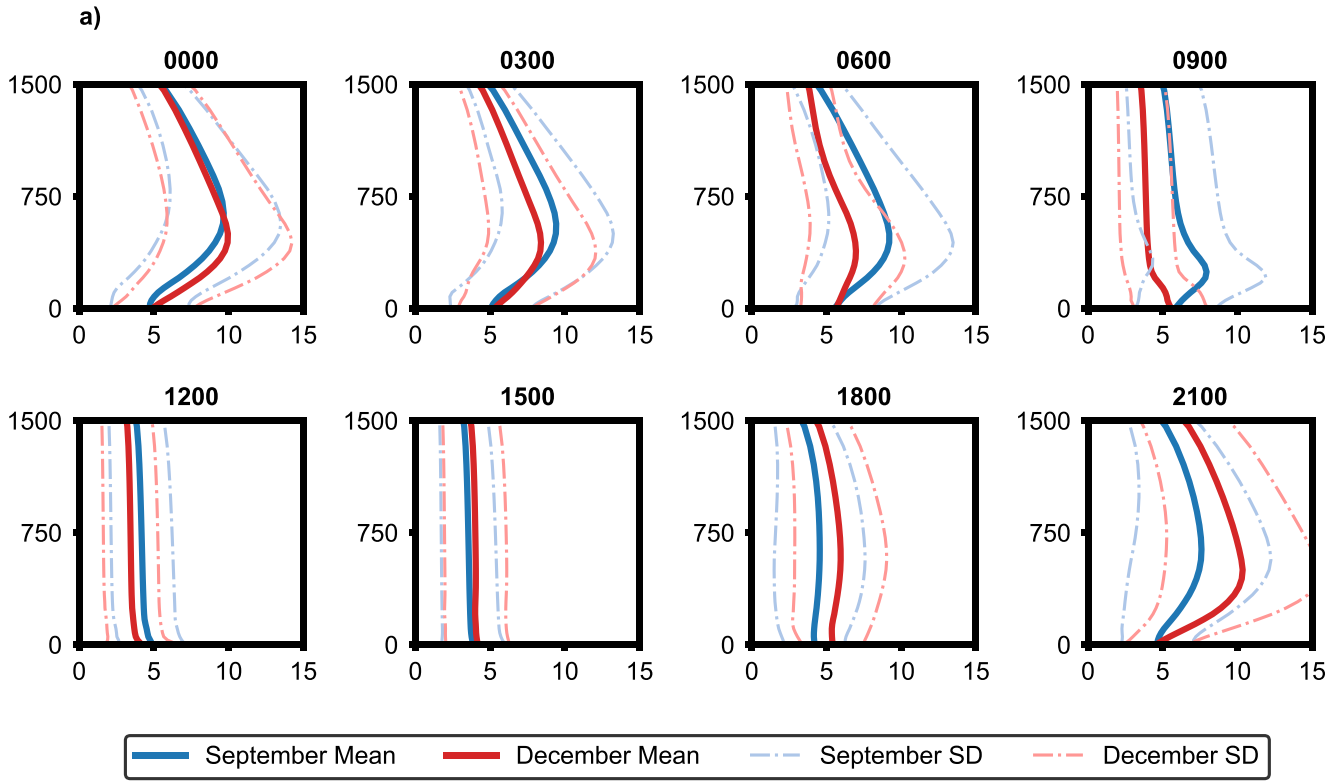

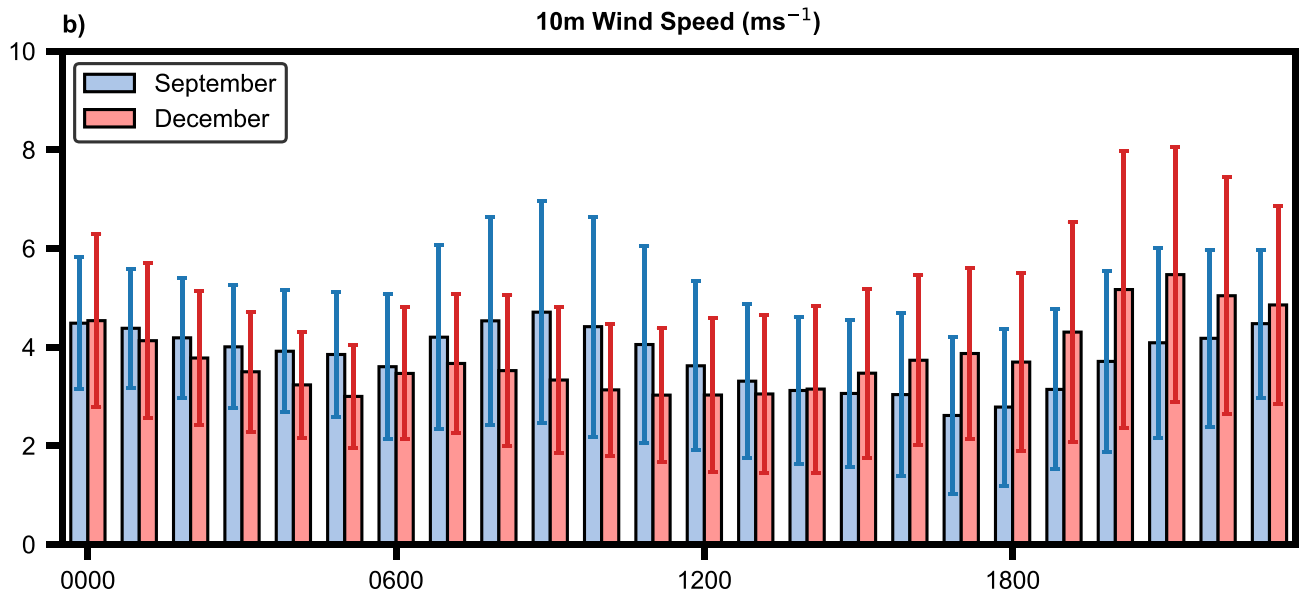

Figure 4. (a) Wind speed-height profiles for high AI September and December composites at Etosha. (b) Diurnal cycle of 10 m wind speed for high AI September and December composites at Etosha. All data from ERA5.

& Washington, 2021; Zunckel et al., 1996). Model level data from ERA5 has also been shown to capture well the main features of the NLLJ at Etosha (Clements & Washington, 2021), and so is a pragmatic choice of reanalysis. The diurnal cycle of 10 m wind speed for the September and December composites are shown in Figure 4b, also constructed from ERA5 data.

A wind speed-height profile akin to a NLLJ is evident in the December composites (Figure 4a), however the timing of its development and breakdown are not consistent with the theory of frictional decoupling typically associated with jets that form in dryland environments (Blackadar, 1957; Fiedler et al., 2013). A jet profile is first observed at 2100, however this is also the time of peak core wind speeds, with the structure beginning to erode long before sunrise (≈0415) and the onset of surface heating. This is in contrast to the evolution of the NLLJ in September, which strengthens through the nocturnal period, peaks in the hours around sunrise (≈0500) and is subsequently eroded with the increase of eddy viscosity in the daytime boundary layer. These contrasts are reflected in the diurnal cycle of surface winds (Figure 4b); in September, there is a peak between sunrise and midday (≈0900) associated with the mix-down of momentum from the NLLJ as it is eroded, however no such peak is evident in December. Instead, surface wind speeds increase during the evening and peak at 2100, around the time at which the jet profile is also at its strongest (Figure 4a).

4.2. Austral Summer Dust Event Case Study: 19 December 1987

The findings presented in Section 4.1 suggest that processes other than the mix-down of momentum from a NLLJ are responsible for driving dust emission at Etosha during December. In order to further investigate, Figures 5 and 6 present ERA5 data from midday on 18 December 1987 to midday on 19 December 1987; the 19 December (AI = 3.3) is the second dustiest December date in the TOMS record and the joint second dustiest date for any month. Figure 5 shows time-height cross sections of wind speed, u, v, temperature and specific humidity at Etosha, whilst Figure 6 shows 10 m wind speed and vectors for a selected area of southern Africa.

Peak wind speeds (>15 ms^{-1}) are recorded at Etosha during the evening of the 18 December in a core ≈300–500 m above the surface (Figure 5a). This is consistent with the December composites shown in Figure 4a, which also displayed a core of enhanced wind speeds at ≈500 m peaking in the 2100 profile. This flow is associated with an integrated sea breeze-topographic wind (hereinafter referred to as an anabatic-sea breeze) which develops along the Namib coast from 1200 on the 18 December, and propagates inland to reach Etosha by 2100 on the same evening (Figure 6). By the time the sea breeze front has reached Etosha, the flow has been deflected by Coriolis to give a large southerly component (Figure 5c), and the arrival of air from the Atlantic is accompanied by a drop in temperature (Figure 5d) and sharp increase in the moisture content of the atmosphere (Figure 5e). The inland propagation of the sea-breeze front provides the only intensification of surface wind speeds at Etosha prior to the TOMS signal on the 19 December (Figure 6), and is a plausible atmospheric driver of summer dust emissions.

5. Climatology of Dust Emission Mechanisms at Etosha

The following sections address key question c: What are the spatial and temporal characteristics of the dust emission mechanisms operating at the Etosha Pan, and what controls their variability?

5.1. Annual Cycle

Figures 7 and 8 show seasonal climatologies of 10 m wind speed and 2 m temperature respectively, for selected areas of southern Africa, both constructed from ERA5 data. OLR contours are also included on Figure 8. The mix-down of momentum from a NLLJ is evident at 0600 and 1200 during winter (JJA) and is manifest as a region of enhanced wind speeds across northern Namibia, embedded within the prevailing anticyclonic flow around southern Africa (Figure 7). A detailed analysis of the characteristics of the NLLJ and the controls on its variability has been given by Clements and Washington (2021), and so is not addressed any further in this section.

The anabatic-sea breeze system is present throughout the year, however its strength and the extent of its inland propagation varies considerably by season. In autumn (MAM) and winter, when diabatic heating over the interior of southern Africa is at a minimum (Figure 8), the system is confined to the coastal plains of the Namib below the level of the escarpment, and can be seen as a slight onshore rotation of the trade winds at 1200 and 1800 (Figure 7). Also prominent during winter along the escarpment is an easterly katabatic-land breeze that develops through the nocturnal period (0000) and is at its strongest in the early morning (0600).

As the area of maximum diabatic heating moves south over the central plateau during spring (SON) (Figure 8), the anabatic-sea breeze system strengthens, and subsequently peaks in intensity during summer (DJF) (Figure 7). At this time of year, the area of maximum diabatic heating is over the southern Kalahari and Northern Cape region

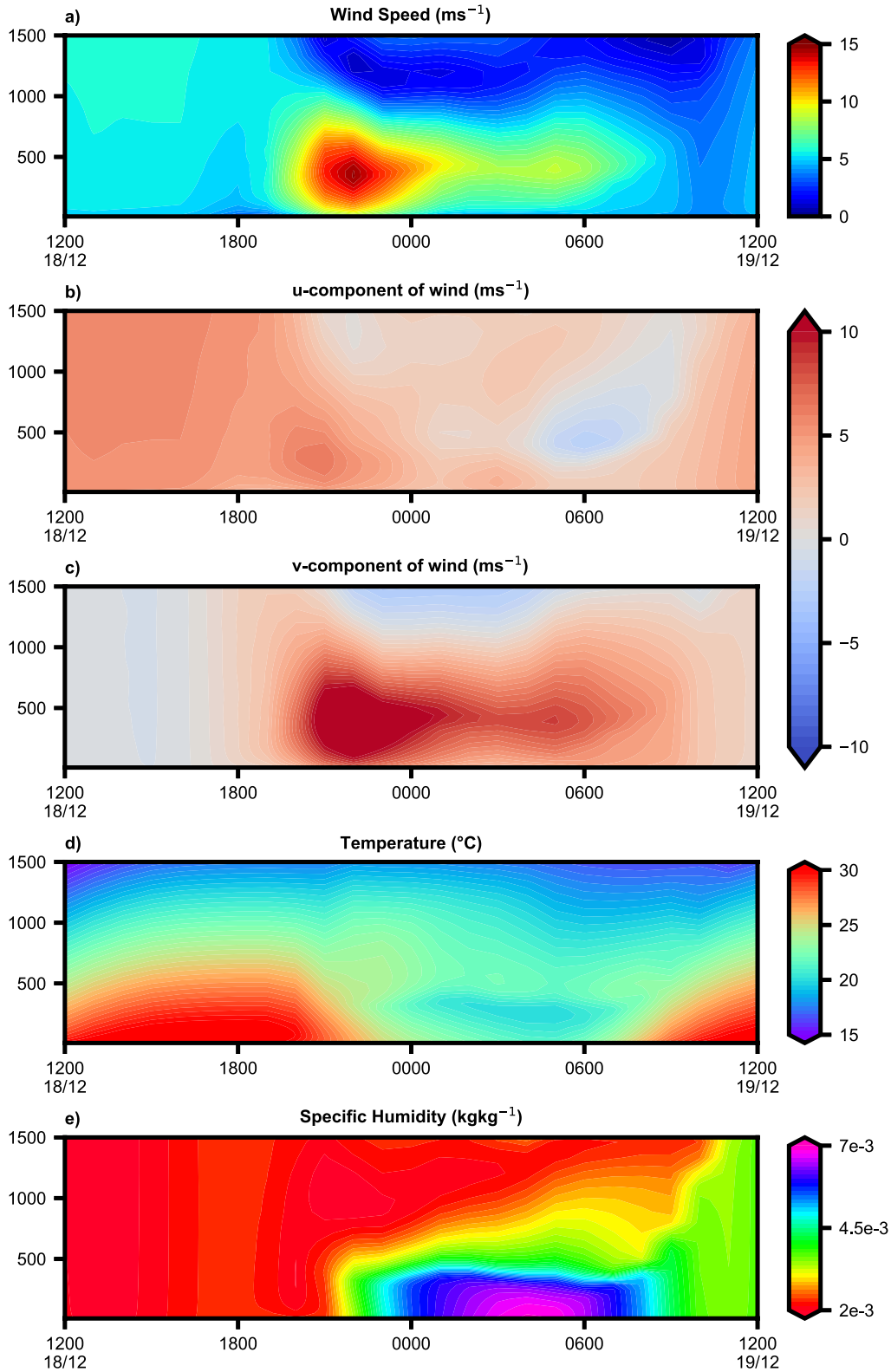

Figure 5. Time-height cross sections of (a) wind speed, (b) u, (c) v, (d) temperature and (e) specific humidity for the period 1200 18 December 87–1200 19 December 87 at Etosha. The 19 December is the second dustiest December date in the Total Ozone Mapping Spectrometer record. All data from ERA5.

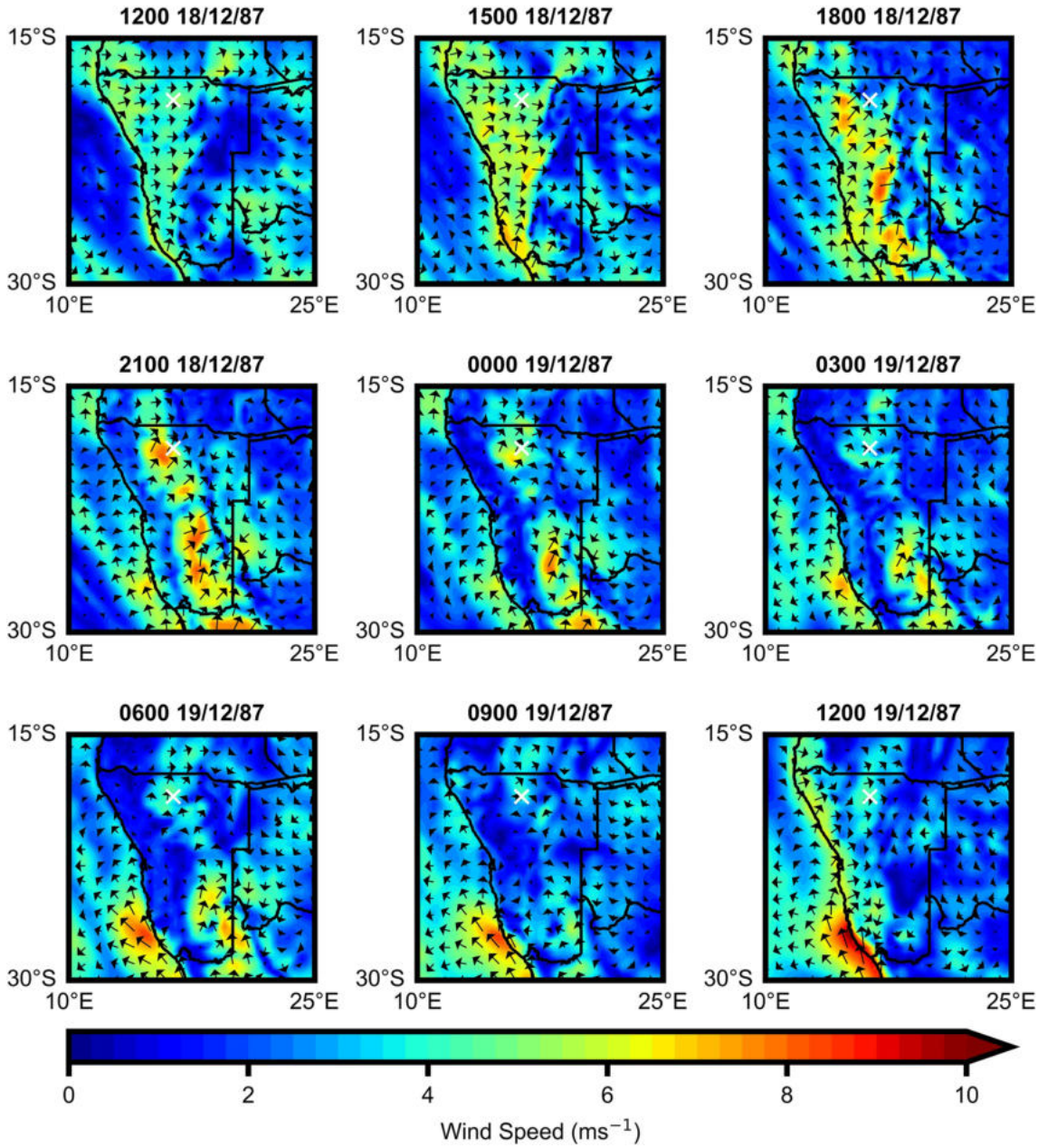

Figure 6. 10 m wind speed and vectors for the period 1200 18 December 87–1200 19 December 87. Etosha's location is given by the white cross. The 19 December is the second dustiest December date in the Total Ozone Mapping Spectrometer record. All data from ERA5.

of South Africa, establishing a strong thermal contrast between the warm, elevated plateau, and the relatively cool waters of the Benguela Upwelling System (BUS). The BUS extends from the southwestern tip of South Africa to the Angola-Benguela Front (ABF) (≈15°S–17°S), with south-easterly wind stress imparted by the trade winds and subsequent offshore Ekman transport driving upwelling of nutrient-dense waters from below the thermocline (Colberg & Reason, 2006; Reason, 2017). The annual cycle of sea surface temperatures (SSTs) lags the latitudinal shift in diabatic heating (Figure 8), so that maximum SSTs are recorded in the BUS from February–March (when interannual variability in the position of the ABF is also at a maximum (Florenchie et al., 2004)); in the early summer months (e.g., December), conditions are therefore optimal for the development of the anabatic-sea breeze south of the ABF, with intense heating of the interior plateau coupled with relatively cool SSTs. After setting in at the coast by midday, the system propagates inland through the afternoon, so that by 1800, a 300 km-wide band of south-westerly winds associated with the anabatic-sea breeze stretches from southern Angola to the Karoo

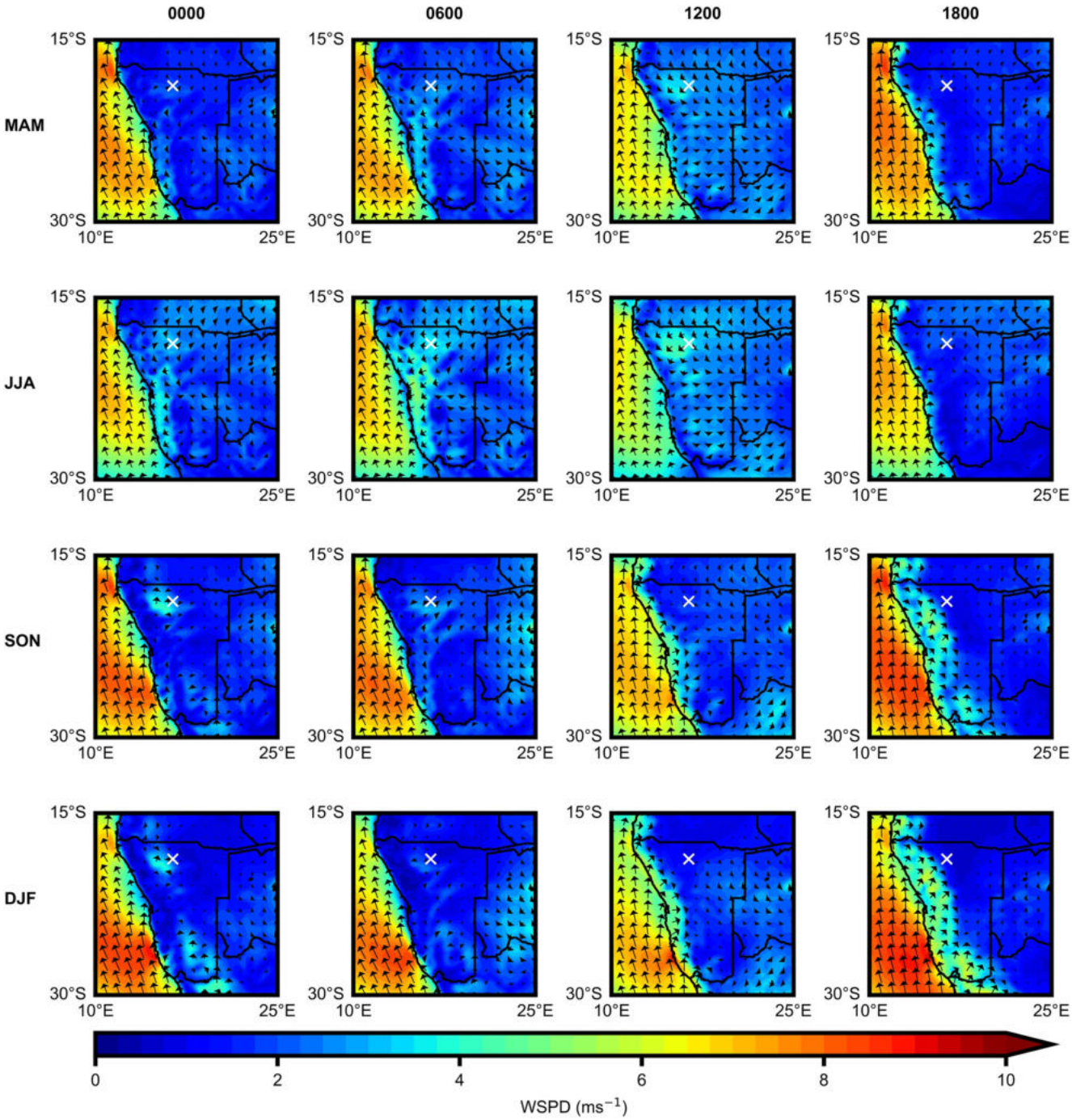

Figure 7. Seasonal climatologies (1981–2010) of 10 m wind speed and vectors for 0000, 0600, 1200, and 1800. Etosha's location is given by the white cross. All data from ERA5.

Desert. Through the evening, the sea breeze front separates from the coast as it continues to move inland, and can be observed in a number of preferential latitudinal bands by 0000.

5.2. Spatial and Temporal Characteristics in Austral Summer

In order to further examine the structure of the anabatic-sea breeze and its diurnal evolution, this section focuses on its characteristics during summer, the season in which it is best developed. Figures 9 and 10 show DJF climatologies of zonal wind and divergence/convergence (contours), plotted as latitude-height and

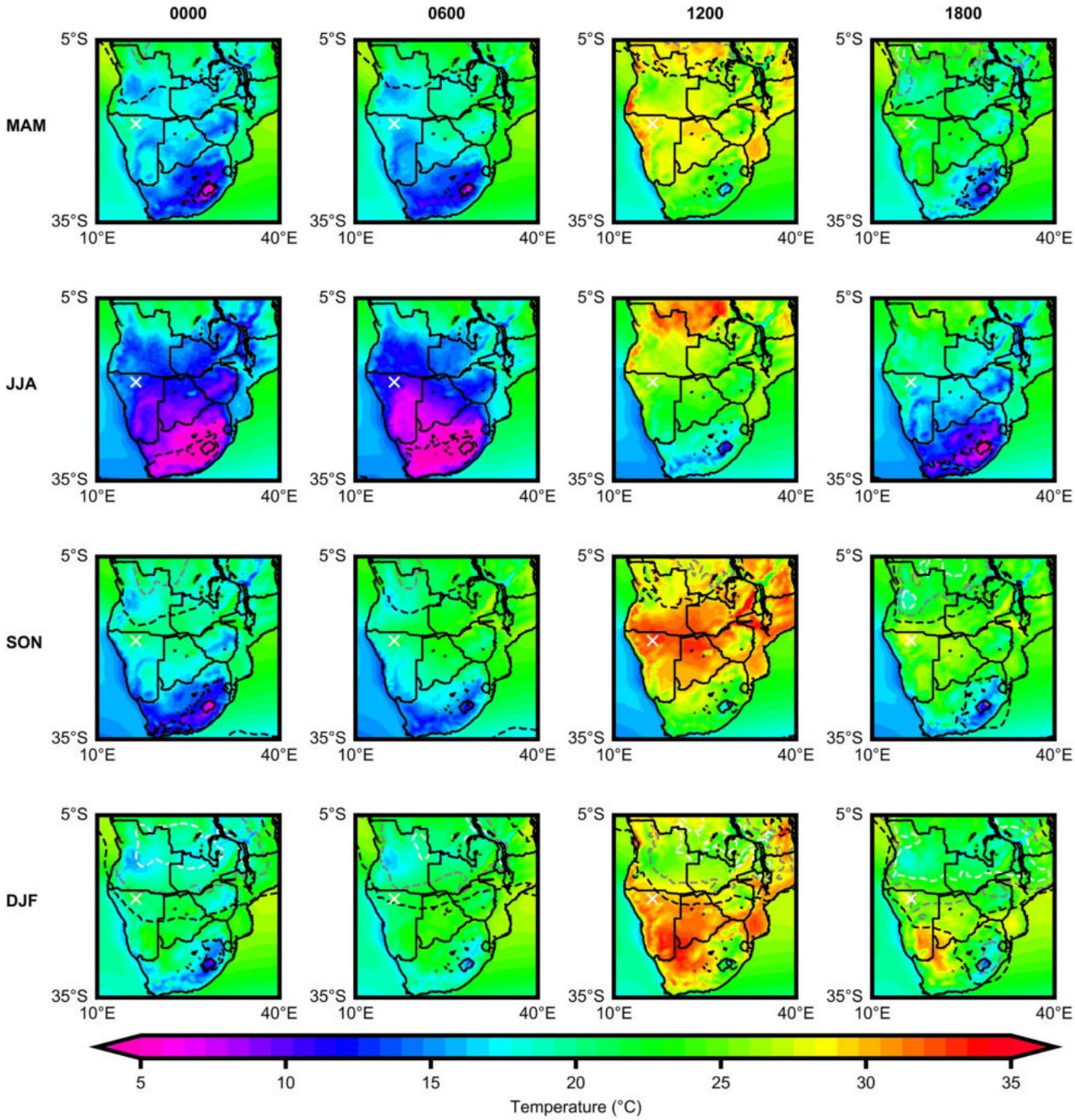

Figure 8. Seasonal climatologies (1981–2010) of 2 m temperature and outgoing longwave radiation (OLR) for 0000, 0600, 1200, and 1800. OLR contours are plotted at 200 Wm^{-2} (white), 225 Wm^{-2} (gray) and 250 Wm^{-2} (black). Etosha's location is given by the white cross. All data from ERA5.

longitude-height respectively. In some instances, the meridional component of the flow associated with the anabatic-sea breeze will be greater than the zonal component (e.g., as it propagates inland and is deflected by the Coriolis force), however it is the positive zonal wind that distinguishes the system from the background flow over southern Africa and the trade winds over the south Atlantic, which are both easterly in nature. Hence, for the purposes of identifying the anabatic-sea breeze, the choice of zonal wind in these plots is pragmatic. Figure 11 shows latitude-height DJF climatologies of temperature and potential-temperature (contours).

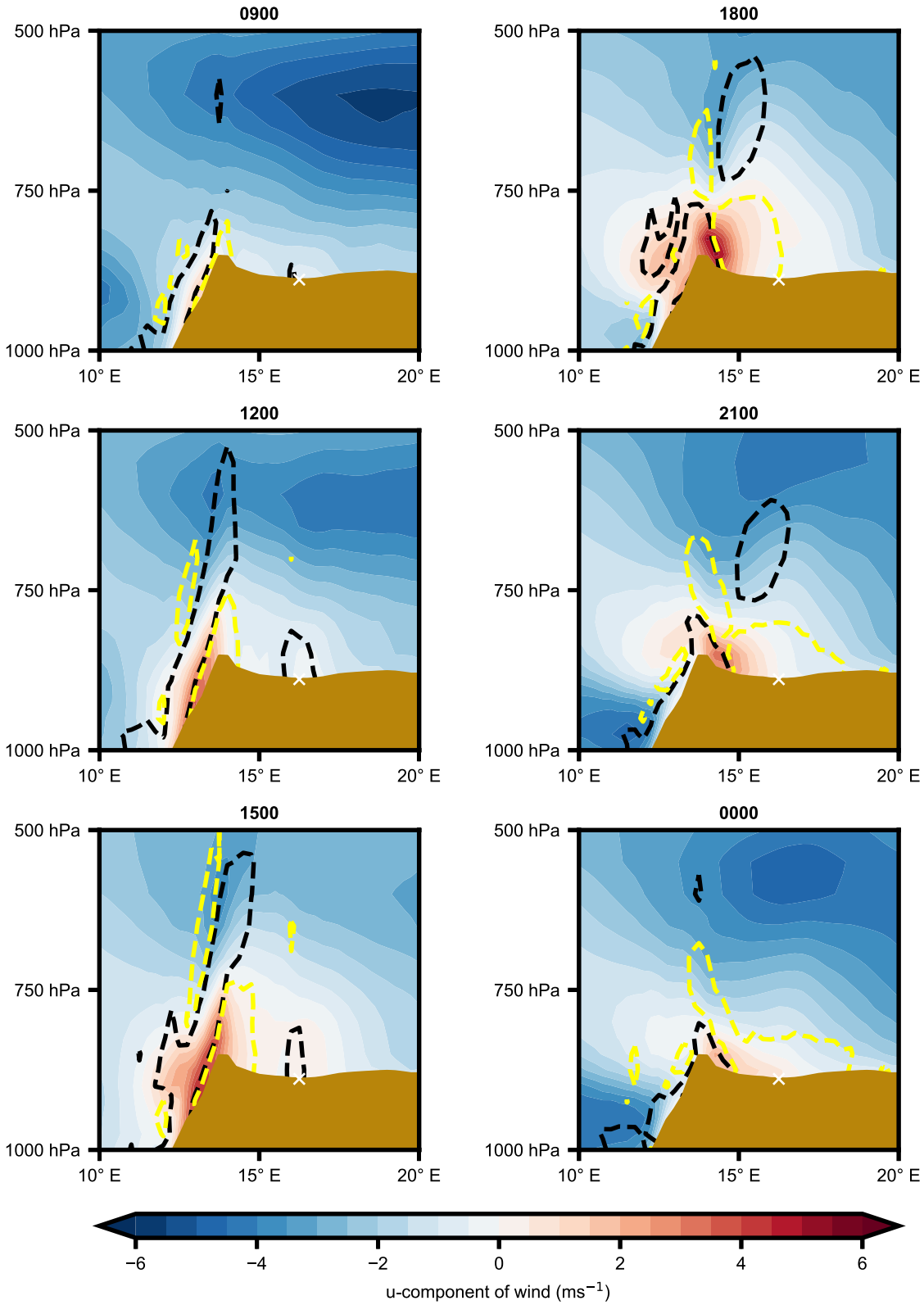

Figure 9. Longitude-height cross section climatology (1981–2010) for DJF of the zonal wind component and divergence (convergence). Areas of divergence (convergence) greater than (less than) 1.0×10^{-5} s^{-1} (-1.0×10^{-5} s^{-1}) are shown by the black (yellow) contours. The cross section is plotted at Etosha's latitude (−18.75), with Etosha's longitude given by the white cross. All data from ERA5.

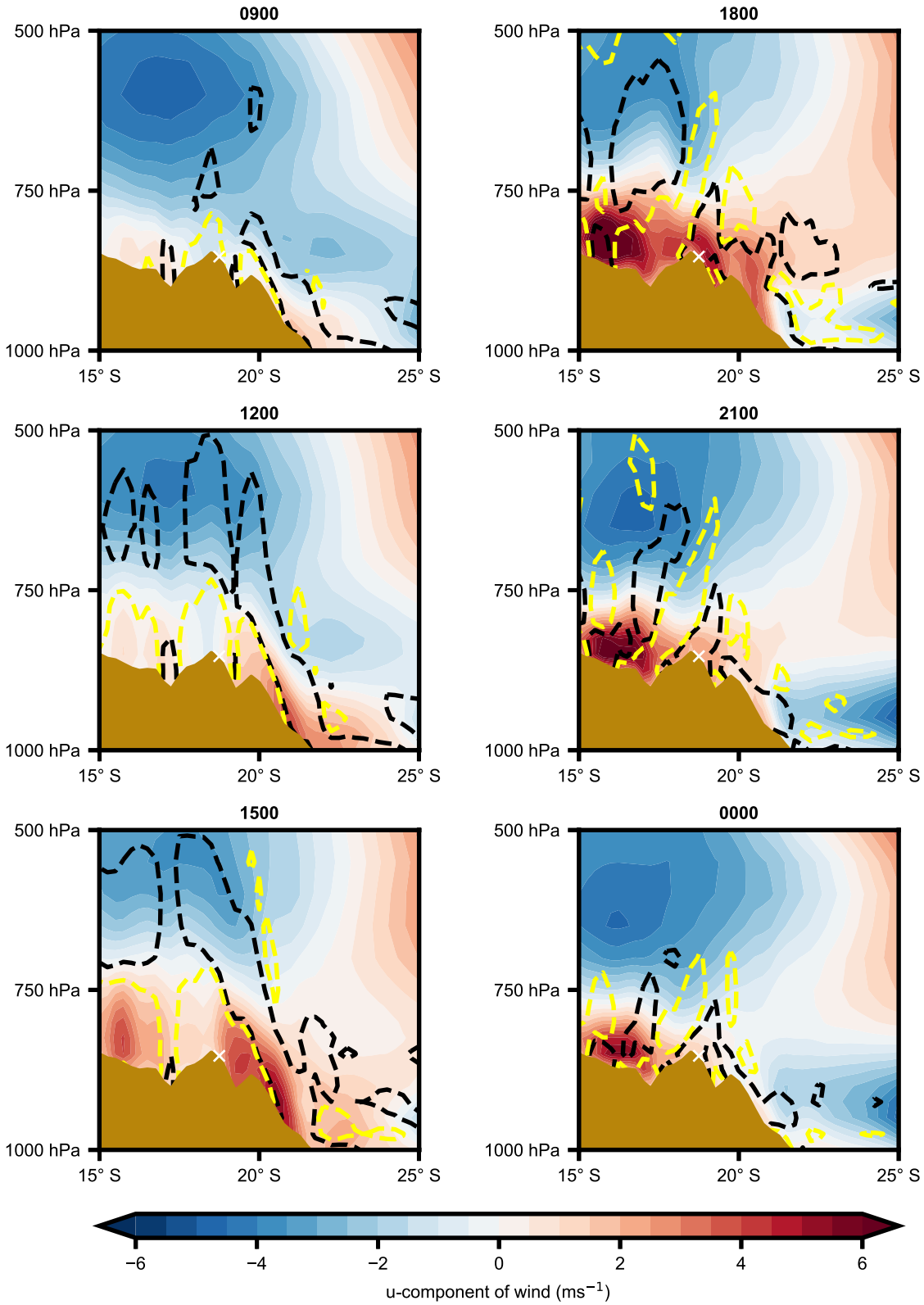

Figure 10. Latitude-height cross section climatology (1981–2010) for DJF of the zonal wind component and divergence (convergence). Areas of divergence (convergence) greater than (less than) 1.0×10^{-5} s^{-1} (-1.0×10^{-5} s^{-1}) are shown by the black (yellow) contours. The cross section is plotted at 14°E, with Etosha's latitude given by the white cross. All data from ERA5.

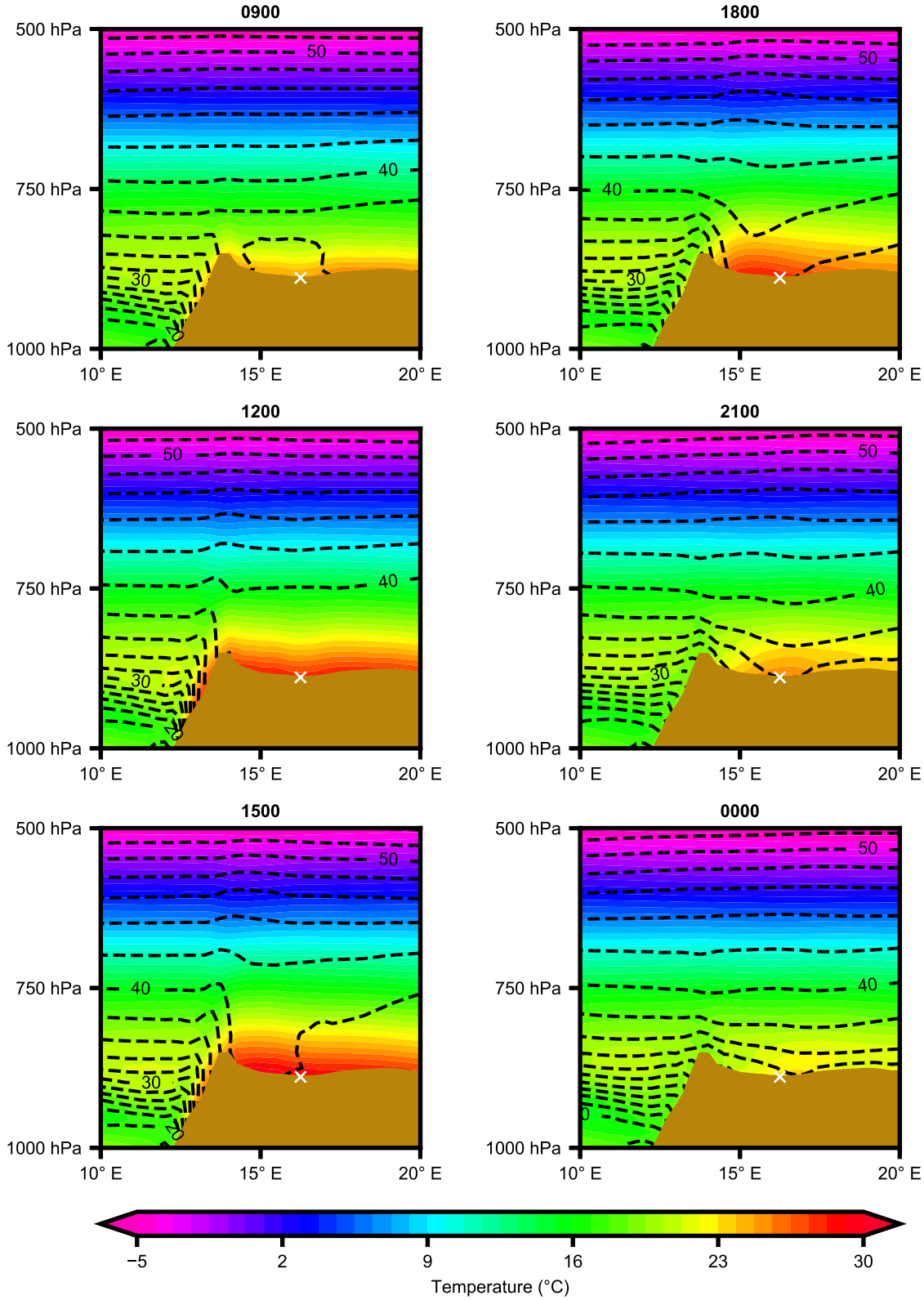

Figure 11. Longitude-height cross section climatology (1981–2010) for DJF of temperature and potential temperature (contours). The cross section is plotted at Etosha's latitude (−18.75), with Etosha's longitude given by the white cross. All data from ERA5.

The anabatic-sea breeze sets in at the coast by 0900 (Figure 9) and strengthens during the morning and early afternoon, so that by 1500 the system presides through the lowest ≈250 hPa of the atmosphere. A plume of divergence is evident up to ≈550 hPa as the flow is accelerated up the escarpment (≈1400 m at Etosha's latitude), with an area of convergence in its immediate lee as the flow is decelerated by friction with the surface. The establishment of the anabatic-sea breeze is a direct response to the uneven diabatic heating of the landmass and the adjacent ocean (Figure 11); at 850 hPa (just above the surface) a zonal gradient in temperature exists at 0900, and is at its most pronounced at 1,500 (when the anabatic-sea breeze is best developed). The daytime profiles of potential temperature are consistent with the modeling work of Smith and Spengler (2011), with a well-mixed layer over the landmass (potential temperature constant with height), and a strong zonal gradient close to the coast (12°E–14°E) demarking the position of the sea breeze front.

Through the afternoon, the anabatic-sea breeze and its associated areas of divergence and convergence propagate inland (Figure 9) so that by 1800, the system has deteriorated below the level of the escarpment, and the topographically generated plume of divergence has collapsed. As the anabatic-sea breeze continues to move inland, it is deflected by the Coriolis force, producing a rotation of the wind vectors from westerly to south-westerly (Figure 7), hence diminishing the zonal component of the flow as it propagates eastwards (Figure 9). The varying extent of the systems inland propagation at different latitudes is partly a consequence of the topography of the Namib coastline, which features deeply incised river valleys running from east-west. These act to channel the anabatic-sea breeze and accelerate the flow, an effect that is illustrated by the structure of the zonal wind contours in Figure 10. The sea-breeze front is therefore evident in a select number of latitudinal bands at 0000 (Figure 7); one south of ≈25°S and another at ≈19°S, coincident with the location of the Etosha Pan.

The persistence of the system at Etosha's latitude is due to the Hoanib River valley, and is illustrated by the enhanced zonal wind component in the topographic low to the south of Etosha's location at 1500 and 1800 (Figure 10). Topographic channeling of winds has been observed along other Namib river valleys, with maximum flow enhancement recorded downwind of the valley edge (Vickery & Eckardt, 2013; Wiggs et al., 2002). Local scale, north-westerly valley winds can also develop during the daytime independent of the anabatic-sea breeze system (Lindesay & Tyson, 1990), further aiding the inland propagation of the onshore flow.

6. Variability in Austral Summer Dust Emissions at Etosha

The following sections address key question d: How does variability in the processes described in Section 5 help to account for variability in austral summer dust emissions from the Etosha Pan?

6.1. Variability in Dust Emission Mechanisms

Figure 12 shows composite diurnal cycles of 10 m wind speed and 2 m temperature at Etosha for the three dustiest (1987, 1989, 1992) and three least dusty (1986, 1988, 1991) December months (Table 2). Both composites show an increase in surface wind speed from 1800 onwards (Figure 12a), with peak values recorded at 2100 and 2000 in the high and low AI years respectively. Results for unpaired, one-tailed *t*-tests, testing for difference in the high and low AI mean wind speeds are presented in Table 3. Significant differences were found for all hours at $\alpha = 0.05$, and for all hours from 1200–0600 at $\alpha = 0.01$, with a much greater peak in the high AI years (5.47 ± 2.58 ms^{-1}) compared to the low AI (3.40 ± 2.02 ms^{-1}). Time-height cross sections of wind speed, u and v at Etosha for high AI, low AI and difference composites are shown in Figure 13; a stronger flow is recorded through the lowest ≈1 km of the atmosphere in the dustiest December months (Figure 13c), with a core of enhanced wind speeds in excess of 10 ms^{-1} developing at ≈400 m from 1800 onwards in the high AI composite (Figure 13a).

The relative strength of the flow at Etosha through the evening hours in the dustiest December months is the result of a better developed anabatic-sea breeze system. Figure 14 shows high AI, low AI and difference composites of 10 m wind speed and vectors for a selected area of southern Africa. As the anabatic-sea breeze develops at the coast through the afternoon (1200 and 1500), it is stronger in the high AI years, especially north of ≈23°S, whilst the background easterly flow over the interior of southern Africa is weaker, aiding the subsequent inland propagation of the system. By 1800, the sea breeze front has almost arrived at Etosha in the high AI composite, consistent with the timing of increasing wind speeds presented in Figures 12a and 13a. In the low AI composite, the system begins to dissipate much earlier at Etosha's latitude, with a weak front evident ≈80 km west of the pan at 2100.

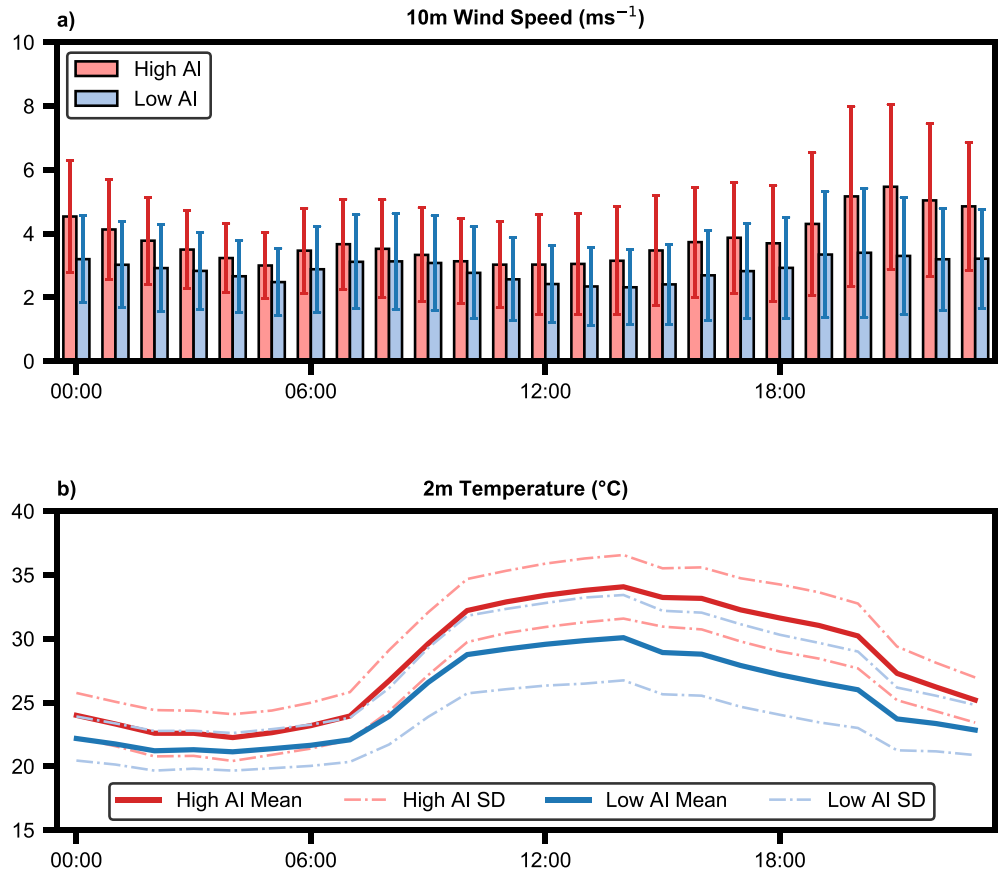

Figure 12. Composite diurnal cycle of (a) 10 m wind speed and (b) 2 m temperature for high AI and low AI December months at Etosha. All data from ERA5.

Table 3
Results of T-Test Calculations Performed on High and Low AI December Hourly Composite Surface Wind Speeds

Time	WS (ms^{-1}) High AI	WS (ms^{-1}) Low AI	t-stat	p-value	t-crit ($\alpha = 0.05$)	t-crit ($\alpha = 0.01$)
0000	4.54	3.20	5.76	1.84×10^{-8}	1.65	2.35
0200	3.78	2.92	4.29	1.45×10^{-5}	1.65	2.35
0400	3.23	2.66	3.51	2.81×10^{-4}	1.65	2.35
0600	3.47	2.88	2.95	1.78×10^{-3}	1.65	2.35
0800	3.52	3.13	1.76	4.03×10^{-2}	1.65	2.35
1000	3.13	2.77	1.77	3.91×10^{-2}	1.65	2.35
1200	3.03	2.42	2.96	1.73×10^{-3}	1.65	2.35
1400	3.15	2.32	3.87	7.93×10^{-5}	1.65	2.35
1600	3.73	2.69	4.47	6.91×10^{-6}	1.65	2.35
1800	3.70	2.93	3.06	1.26×10^{-3}	1.65	2.35
2000	5.17	3.40	4.89	1.19×10^{-6}	1.65	2.35
2200	5.04	3.20	6.14	3.09×10^{-9}	1.65	2.35

6.2. Controls on Variability

The differences in the strength of the anabatic-sea breeze between high and low AI Decembers outlined in Section 6.1 can be accounted for by considering the pattern of diabatic heating over the interior of southern Africa, a process that was identified as a key control on the development of the system in Section 5. Figure 15 shows high AI, low AI and difference composites of 2 m temperature and OLR for a selected area of southern Africa. Diabatic heating is stronger in the high AI composite across the southern Kalahari/Northern Cape region identified in Section 5.1 as critical to the development of the anabatic-sea breeze, however there is a more substantial difference in heating between the two composites across northern Namibia and southern Angola (Figure 15). This is also reflected in the diurnal cycle of temperature at Etosha (Figures 12b and 13j–13l), with an ≈ 4°C difference in surface temperature between the high and low AI composites at 1400 (Figure 12b).

The contrast in diabatic heating is the result of a south-westward shift in the area of tropical convection during the low AI years, illustrated by the OLR contours in Figure 15, and a moistening of the atmosphere at Etosha (Figures 13m–13o). This acts to disrupt the pattern of diabatic heating, especially across northern Namibia and southern Angola, and helps to explain the inability of the anabatic-sea breeze to propagate as far inland at Etosha's latitude. Benguela Niños, characterized by positive SST anomalies along the Namib-Angolan coastline (Florenchie et al., 2004; Rouault, 2012), as well as

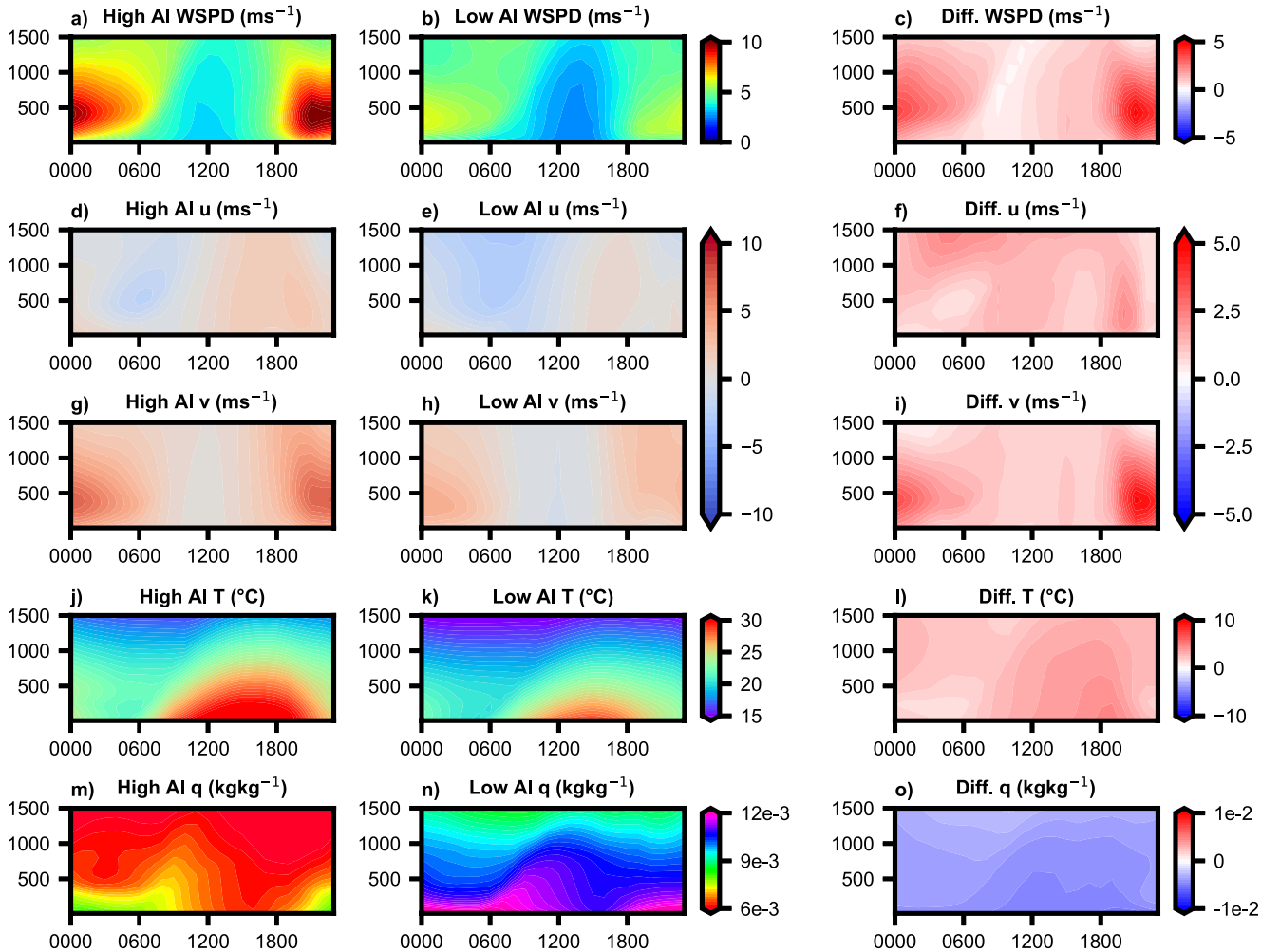

Figure 13. Time-height cross sections of (a–c) wind speed, (d–f) u, (g–i) v, (j–l) temperature and (m–o) specific humidity for December high AI, low AI and difference composites at Etosha. The difference composites were calculated by subtracting the low AI from the high AI. All data from ERA5.

La Niña events, which are associated with a strengthening of the Angola Low (Howard & Washington, 2018), could both drive the observed shift in tropical convection in the low AI composites; indeed, the low AI (1.3) December of 1988 was contemporaneous with a strong La Niña event in the tropical Pacific, for example, The timing of these events does not necessarily coincide with low AI December months however, with for instance the December of 1986 (AI = 1.3) concurrent with negative SST anomalies in the eastern Atlantic (Florenchie et al., 2004).

7. Discussion and Conclusion

This paper has utilized TOMS AI and ERA5 reanalysis data in order to investigate the atmospheric controls on dust emission from the Etosha Pan throughout the annual cycle. Four key questions were posed in the introduction: (a) What is the annual cycle of dust emissions from the Etosha Pan? (b) How do the atmospheric processes responsible for driving dust emission from the Etosha Pan vary through the annual cycle? (c) What are the spatial and temporal characteristics of the dust emission mechanisms operating at the Etosha Pan, and what controls their variability? (d) How does variability in the processes described help to account for variability in austral summer dust emissions from the Etosha Pan? The results presented in Sections 3–6 will now be discussed, and the main findings of the paper summarized, addressing each of the key questions in turn.

Mean AI data for the Etosha Pan shows a peak in dust emissions in September (AI = 1.7) (Figure 1, Table 1), however unlike at Makgadikgadi, southern Africa's other major source area, AI values remain high at Etosha

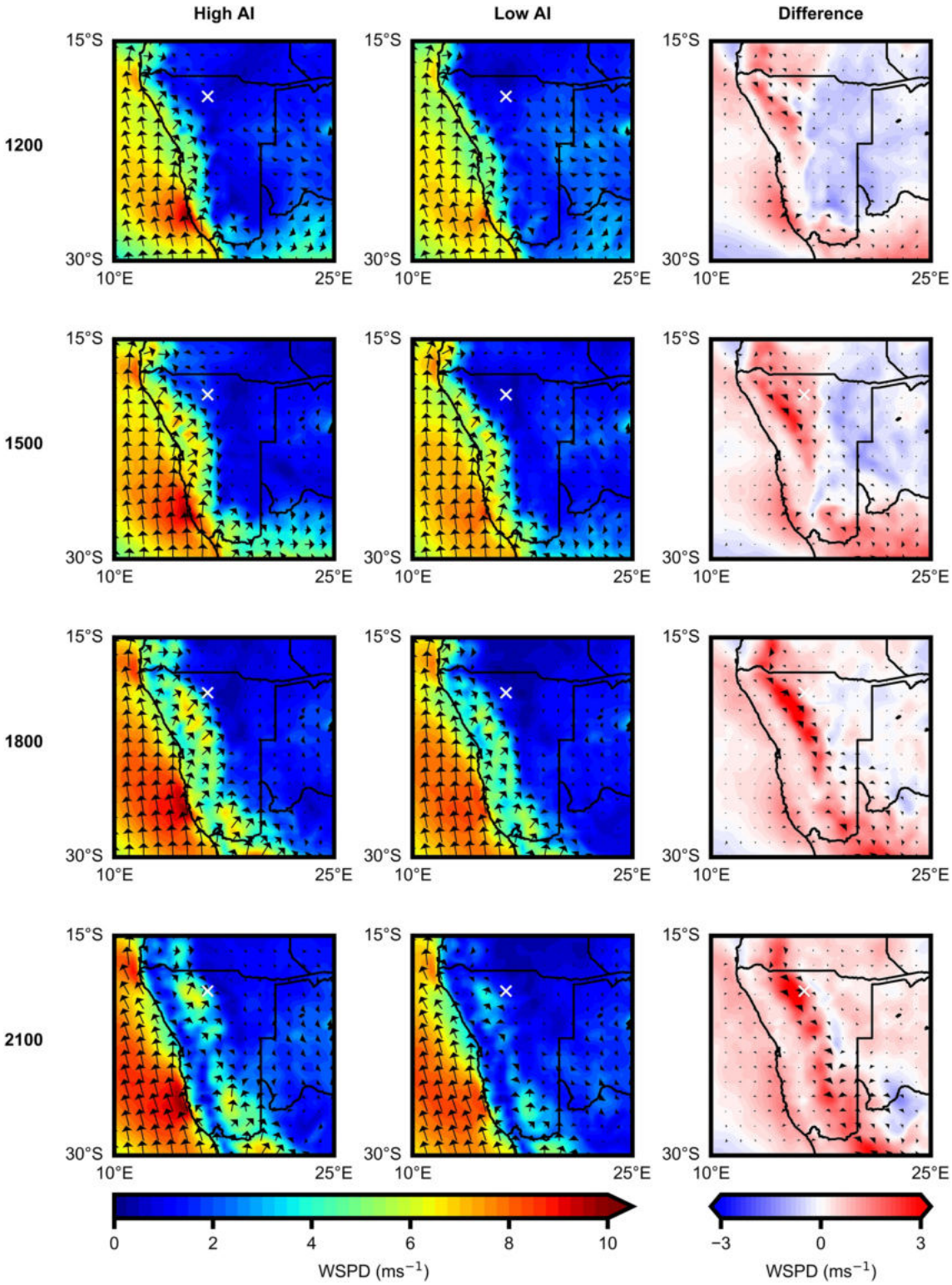

Figure 14. December high AI, low AI and difference composites of 10 m wind speed and vectors. Etosha's location is given by the white cross. The difference composites were calculated by subtracting the low AI from the high AI. All data from ERA5.

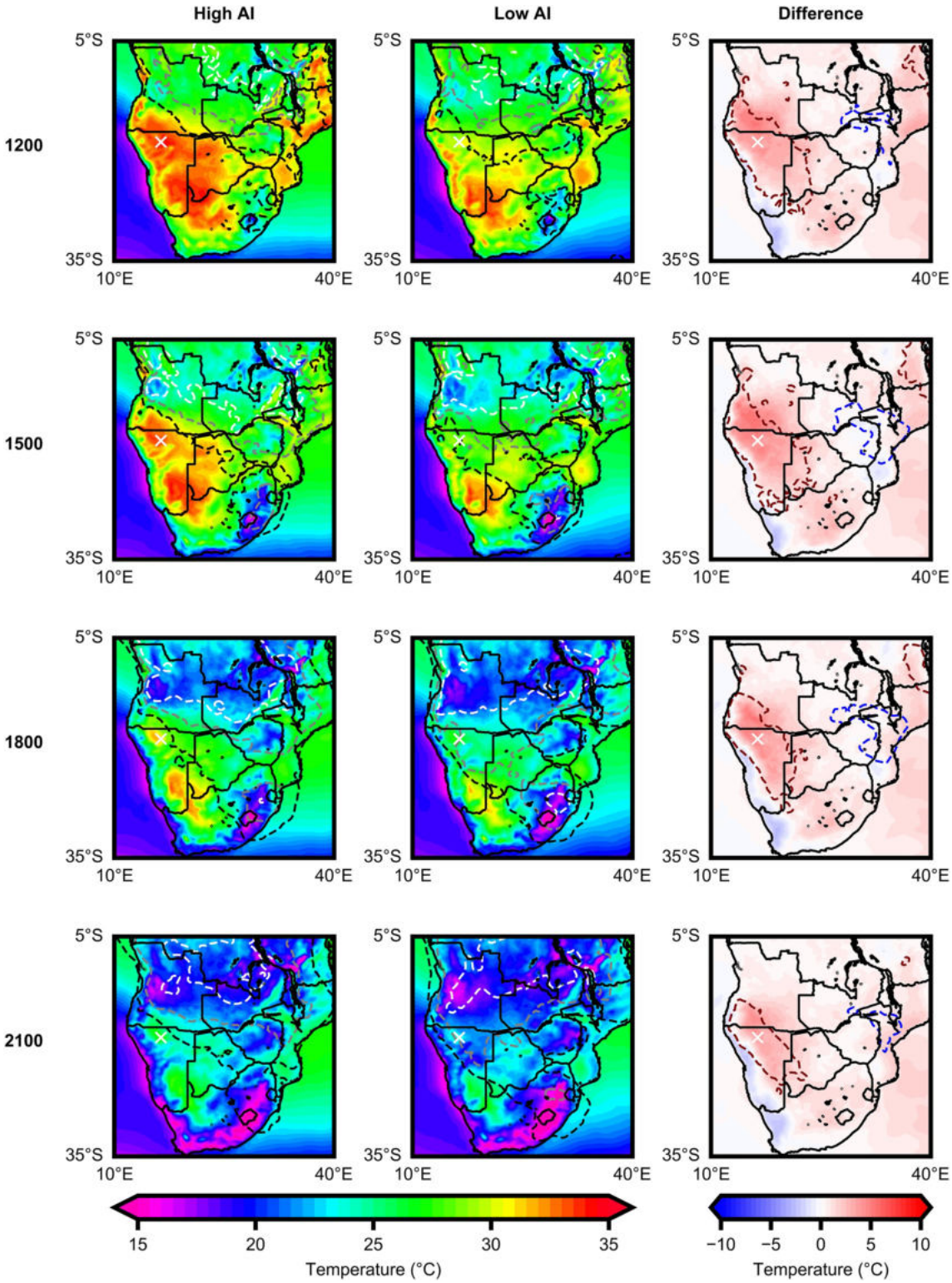

Figure 15. December high AI, low AI and difference composites of 2 m temperature and outgoing longwave radiation (OLR). In the high AI and low AI composites, OLR contours are plotted at 200 Wm^{-2} (white), 225 Wm^{-2} (gray) and 250 Wm^{-2} (black). In the difference composites, the red (blue) contour denotes areas with $a + 25$ Wm^{-2} (-25 Wm^{-2}) difference. Etosha's location is given by the white cross. The difference composites were calculated by subtracting the low AI from the high AI. All data from ERA5.

through spring and into summer, with a secondary peak recorded in December (AI = 1.6) (key question a). The peak in September is consistent with the findings of other remote sensing studies (Prospero et al., 2002; Washington et al., 2003), including those utilizing other satellite data (Vickery et al., 2013), however the dust activity observed during summer has received relatively little attention, and hence was the focus of much of this paper. Precipitation composites showed greater rainfall in the Etosha catchment in the low AI December months compared to the high AI months, and very little difference in rainfall in the preceding summer wet season (Figure 3). These results are similar to the findings of Bryant (2003), who showed that inundation events during 1997/98 and 1999/2000 resulted in an immediate reduction of AI values at Etosha.

During the dustiest December months (key question b), surface wind speeds increase through the evening and peak at 2100, whilst a core of enhanced wind speeds develops at ≈400 m and peaks at the same time (Figure 4). This is in contrast to September, with the findings of this study, and previous work utilizing in situ observations at Etosha (Clements & Washington, 2021; Zunckel et al., 1996) showing the typical evolution and breakdown of a NLLJ and associated morning peak in surface winds. These results preclude the possibility of a NLLJ being the primary emission mechanism during summer; indeed, a case study of a dust event (Figures 5 and 6) demonstrates the potential role of an anabatic-sea breeze system that develops along the Namib coast and propagates inland to reach Etosha during the evening, concurrent with the observed peak in surface winds during the dustiest December months.

The anabatic-sea breeze is evident along the Namib coast during all seasons (key question c), however it is strongest during summer, when it also propagates furthest inland (Figure 7). The system is a response to the thermal contrast between the elevated interior plateau of southern Africa, and the cool waters of the BUS, and hence is best developed when the area of maximum diabatic heating is situated over the southern Kalahari/Northern Cape region, and to the south of the ABF (Figure 8). The west coast of the subcontinent south of ≈15°S therefore provides an ideal physical setting for the development of such a system; whilst the topography of the escarpment is not as extreme in the west as it is along the eastern slopes of Natal, there is a much greater thermal contrast in the west owing to the relatively cool waters of the BUS (December mean SST of ≈17°C at 20°S) compared to the warm Agulhas current of the Indian Ocean (December mean SST of ≈27°C at 20°S) (Lindesay & Tyson, 1990). The position of the South Atlantic Anticyclone (SAA), centered at ≈ 30°S, 5°W in austral summer, and the anticlockwise rotation of air associated with the high-pressure cell gives south-easterlies along the southwest coast of southern Africa; the stress imparted by these surface winds drives offshore Ekman transport and hence the upwelling of cold water from below the thermocline (Colberg & Reason, 2006; Reason, 2017). The inland propagation of the anabatic-sea breeze is facilitated at Etosha's latitude by the presence of the Hoanib River valley (Figure 10), with topographic channeling of winds a process that has been observed in some of Namibia's other ephemeral rivers (Vickery & Eckardt, 2013; Wiggs et al., 2002).

Surface wind speeds at Etosha are significantly stronger in the dustiest December months when compared to the least dusty (Figure 12, Table 3) (key question d), a manifestation of a better developed anabatic-sea breeze (Figure 14). The contrasting strength of the system between the two sets of composites is driven by differences in the pattern of diabatic heating over southern Africa, with a south-westward displacement of the area of tropical convection disturbing the heating over northern Namibia and southern Angola in the low AI years (Figure 15).

Given the predicted future warming across southern Africa (Boucher et al., 2013; Reason, 2017), along with the sensitivity of the anabatic-sea breeze to the degree and location of maximum diabatic heating, there is the potential for longer-term variability in the strength of the system and hence dust emissions at Etosha. In order to explore this possibility, we present 10 m wind speed (Figure 16) and 2 m temperature (Figure 17) anomalies for December, for the previous four decades, against the 1981–2010 climatology. OLR contours are also included on Figure 17.

The anabatic-sea breeze was best developed during the 1980s (Figure 16), with positive wind speed anomalies and westerly vectors coincident with the position of the sea breeze front as it propagates inland through the evening. Despite the general warming trend observed across southern Africa since 1981 (Figure 17), the strength of the anabatic-sea breeze has not changed appreciably; indeed, the system was relatively weak during the last decade, as shown by the negative wind speed anomalies and easterly vectors coincident with the position of the front. This is partly due to the south-westward shift in the area of tropical convection (indicated by the negative OLR anomaly over northern Namibia/southern Angola) which disturbs the pattern of diabatic heating and modulates the degree of warming across a region of southern Africa shown to be crucial to the development of the anabatic-sea breeze (Section 5.1). Another possible explanation for the multi-decadal trends observed in the strength of the system is variability in the position and strength of the SAA, given the role the feature plays in

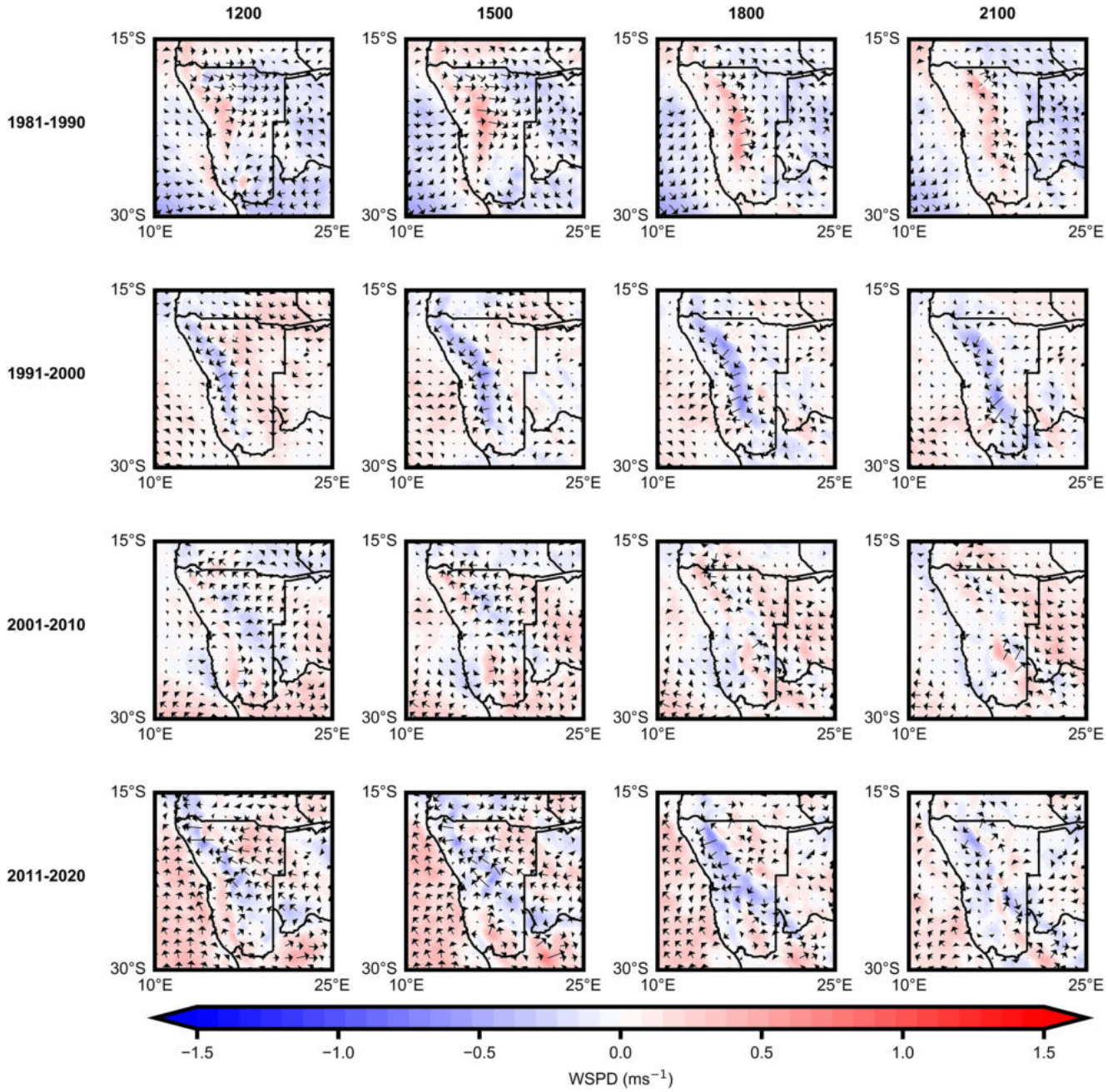

Figure 16. Decadal anomalies of 10 m wind speed and vectors for 1200, 1500, 1800, and 2100, for December, with respect to the 1981–2010 climatology. Etosha's location is given by the white cross. All data from ERA5.

sustaining the BUS and hence the cool SSTs off of the coast of subtropical southern Africa. For example, Venegas et al. (1997) show zonal and meridional oscillations in the position of the SAA with periods of 6–7 and 4 years respectively, whilst Vizy and Cook (2016) report a general poleward shift of the high-pressure cell since the 1980's and a subsequent reduction in upwelling along the Angolan coast.

Whilst the anabatic-sea breeze has been identified in previous work (Howard & Washington, 2018; Lindesay & Tyson, 1990), this is the first time it has been shown to be associated with dust uplift from southern African source areas. Lindesay and Tyson (1990) document the predominance of topographically induced plain-mountain winds, and a thermally induced sea breeze during the daytime in the summer months (both westerly in nature) at a site in the central Namib, with a tendency for these onshore flows to drift inland through the evening. The

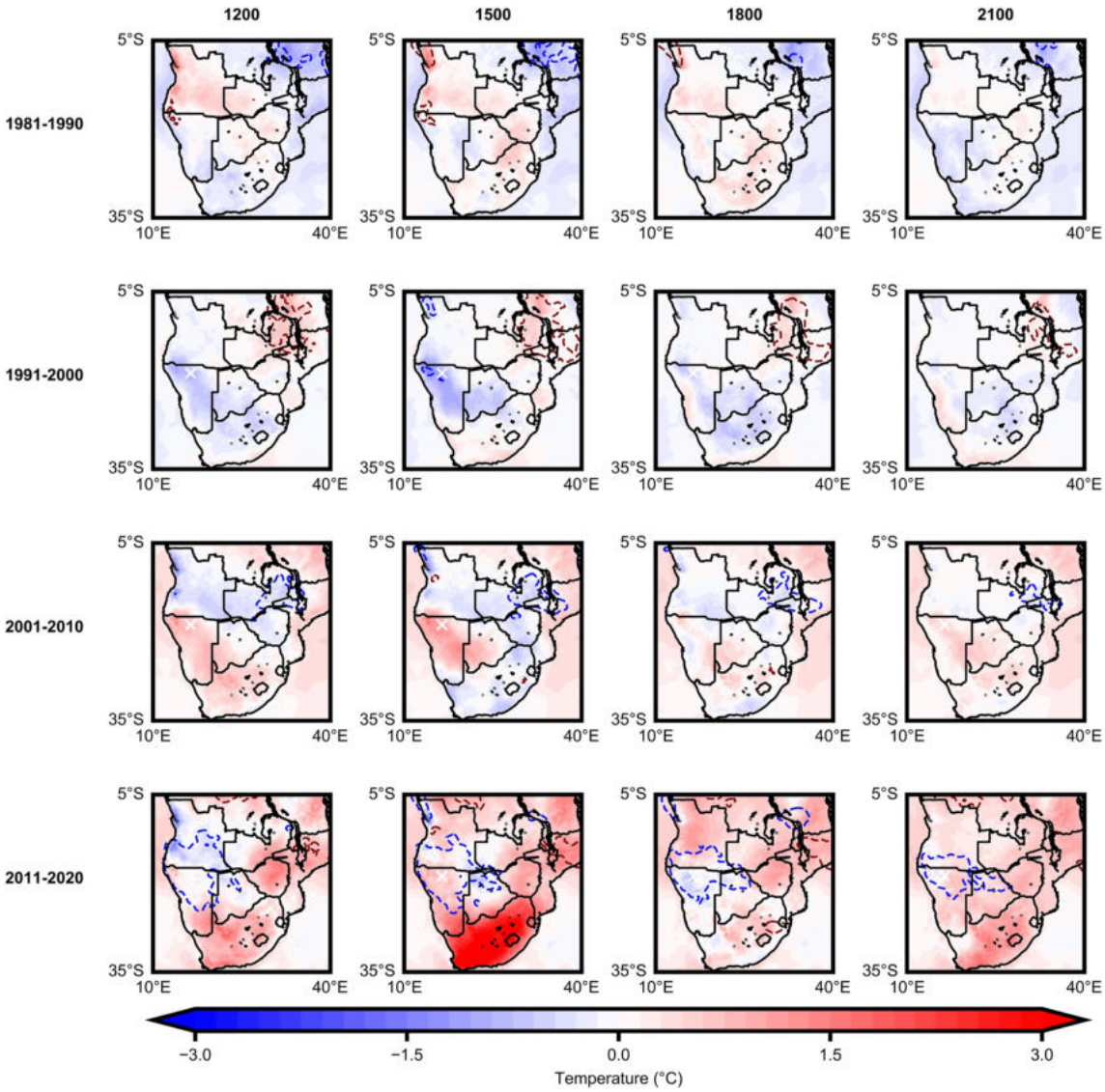

Figure 17. Decadal anomalies of 2 m temperature and outgoing longwave radiation (OLR) for 1200, 1500, 1800, and 2100, for December, with respect to the 1981–2010 climatology. The red (blue) contour denotes areas with $a + 10$ Wm^{-2} (-10 Wm^{-2}) OLR anomaly. Etosha's location is given by the white cross. All data from ERA5.

results presented here suggest that this integrated system is extensive, covering a latitudinal range of up to 15° and propagating up to 5° inland from the coast.

The findings of this study do not preclude other atmospheric processes contributing to summer emissions at Etosha, especially given the importance of convective cold pools in other dust source areas (Allen et al., 2013; Caton Harrison et al., 2019). The inland propagation of the anabatic-sea breeze to Etosha's longitude is contemporaneous with dust uplift from the pan, however it is also plausible that the system plays a key role in triggering convection, which subsequently drives emission from the surface. More work is therefore required, especially across the rest of the summer season, to fully explore the range of atmospheric processes operating at Etosha.

Data Availability Statement

Data—ERA5 data is maintained by ECMWF and is available online from the Copernicus Climate Change Service (CDS, 2018) (https://doi.org/10.24381/cds.adbb2d47). Translation available via browser plug-in. Data—TOMS AI data is available online from the IRI data library (IRI, 1996) (https://iridl.ldeo.columbia.edu/SOURCES/.

NASA/.GSFC/.TOMS/.NIMBUS7/.monthly/.ai/). Translation available via browser plug-in. Data—CHIRPS data is maintained by the Climate Hazards Centre and is available online (CHC, 2014) (https://data.chc.ucsb.edu/products/CHIRPS-2.0/). Translation available via browser plug-in.

Acknowledgments
Matthew Clements is funded by the NERC doctoral training partnership (NE/L002612/1).

References

Allen, C. J. T., & Washington, R. (2014). The low-level jet dust emission mechanism in the central Sahara: Observations from Bordj-Badji Mokhtar during the June 2011 fennec intensive observation period. *Journal of Geophysical Research: Atmospheres*, *119*(6), 2990–3015. https://doi.org/10.1002/2013JD020594

Allen, C. J. T., Washington, R., & Engelstaedter, S. (2013). Dust emission and transport mechanisms in the central Sahara: Fennec ground-based observations from Bordj Badji Mokhtar, June 2011. *Journal of Geophysical Research: Atmospheres*, *118*(12), 6212–6232. https://doi.org/10.1002/jgrd.50534

Bechtold, P., Semane, N., Lopez, P., Chaboureau, J.-P., Beljaars, A., & Bormann, N. (2014). Representing equilibrium and nonequilibrium convection in large-scale models. *Journal of the Atmospheric Sciences*, *71*(2), 734–753. https://doi.org/10.1175/JAS-D-13-0163.1

Blackadar, A. K. (1957). Boundary layer wind maxima and their significance for the growth of nocturnal inversions. *Bulletin of the American Meteorological Society*, *38*(5), 283–290. https://doi.org/10.1175/1520-0477-38.5.283

Boucher, O., Randall, D., Artaxo, P., Bretherton, C., Feingold, G., Forster, P., et al. (2013). Clouds and aerosols. In T. F. Stocker, et al. (Eds.), *Climate change 2013: The physical science basis. Contribution of working group i to the fifth assessment report of the intergovernmental panel on climate change* (pp. 571–657). Cambridge University Press. https://doi.org/10.1017/CBO9781107415324.016

Boussetta, S., Balsamo, G., Beljaars, A., Kral, T., & Jarlan, L. (2013). Impact of a satellite-derived leaf area index monthly climatology in a global numerical weather prediction model. *International Journal of Remote Sensing*, *34*(9–10), 3520–3542. https://doi.org/10.1080/01431161.2012.716543

Bryant, R. G. (2003). Monitoring hydrological controls on dust emissions: Preliminary observations from Etosha pan, Namibia. *The Geographical Journal*, *169*(2), 131–141. https://doi.org/10.1111/1475-4959.04977

Caton Harrison, T., Washington, R., & Engelstaedter, S. (2019). A 14-year climatology of Saharan dust emission mechanisms inferred from automatically tracked plumes. *Journal of Geophysical Research: Atmospheres*, *124*(16), 9665–9690. https://doi.org/10.1029/2019JD030291

Caton Harrison, T., Washington, R., & Engelstaedter, S. (2021). Satellite-derived characteristics of Saharan cold pool outflows during boreal summer. *Journal of Geophysical Research: Atmospheres*, *126*(3), e2020JD033387. https://doi.org/10.1029/2020JD033387

CDS. (2018). ERA5 hourly data on single levels from 1959 to present [Dataset]. Copernicus Climate Change Service (C3S) Climate Data Store (CDS). https://doi.org/10.24381/cds.adbb2d47

CHC. (2014). Climate hazards group infrared precipitation with station data [Dataset]. Climate Hazards Center Data Store. Retrieved from https://data.chc.ucsb.edu/products/CHIRPS-2.0/

Clements, M., & Washington, R. (2021). Atmospheric controls on mineral dust emission from the Etosha pan, Namibia: Observations from the clarify-2016 field campaign. *Journal of Geophysical Research: Atmospheres*, *126*(14), e2021JD034746. https://doi.org/10.1029/2021JD034746

Colberg, F., & Reason, C. J. C. (2006). A model study of the Angola benguela frontal zone: Sensitivity to atmospheric forcing. *Geophysical Research Letters*, *33*(19), L19608. https://doi.org/10.1029/2006GL027463

Evan, A. T. (2018). Surface winds and dust biases in climate models. *Geophysical Research Letters*, *45*(2), 1079–1085. https://doi.org/10.1002/2017GL076353

Evan, A. T., Flamant, C., Fiedler, S., & Doherty, O. (2014). An analysis of Aeolian dust in climate models. *Geophysical Research Letters*, *41*(16), 5996–6001. https://doi.org/10.1002/2014GL060545

Fiedler, S., Schepanski, K., Heinold, B., Knippertz, P., & Tegen, I. (2013). Climatology of nocturnal low-level jets over North Africa and implications for modeling mineral dust emission. *Journal of Geophysical Research: Atmospheres*, *118*(12), 6100–6121. https://doi.org/10.1002/jgrd.50394

Florenchie, P., Reason, C., Lutjeharms, J., Rouault, M., Roy, C., & Masson, S. (2004). Evolution of interannual warm and cold events in the southeast Atlantic Ocean. *Journal of Climate*, *17*(12), 2318–2334. https://doi.org/10.1175/1520-0442(2004)017⟨2318:EOIWAC⟩2.0.CO;2

Funk, C., Peterson, P., Landsfeld, M., Pedreros, D., Verdin, J., Shukla, S., et al. (2015). The climate hazards infrared precipitation with stations—A new environmental record for monitoring extremes. *Scientific Data*, *2*(1), 150066. https://doi.org/10.1038/sdata.2015.66

Garcia-Carreras, L., Marsham, J. H., Parker, D. J., Bain, C. L., Milton, S., Saci, A., et al. (2013). The impact of convective cold pool outflows on model biases in the Sahara. *Geophysical Research Letters*, *40*(8), 1647–1652. https://doi.org/10.1002/grl.50239

Goudie, A. S. (2014). Desert dust and human health disorders. *Environment International*, *63*, 101–113. https://doi.org/10.1016/j.envint.2013.10.011

Haywood, J., & Boucher, O. (2000). Estimates of the direct and indirect radiative forcing due to tropospheric aerosols: A review. *Reviews of Geophysics*, *38*(4), 513–543. https://doi.org/10.1029/1999RG000078

Heinold, B., Knippertz, P., Marsham, J. H., Fiedler, S., Dixon, N. S., Schepanski, K., et al. (2013). The role of deep convection and nocturnal low-level jets for dust emission in summertime West Africa: Estimates from convection-permitting simulations. *Journal of Geophysical Research: Atmospheres*, *118*(10), 4385–4400. https://doi.org/10.1002/jgrd.50402

Herman, J. R., Bhartia, P. K., Torres, O., Hsu, C., Seftor, C., & Celarier, E. (1997). Global distribution of UV-absorbing aerosols from nimbus 7/toms data. *Journal of Geophysical Research*, *102*(D14), 16911–16922. https://doi.org/10.1029/96JD03680

Hersbach, H., Bell, B., Berrisford, P., Hirahara, S., Horányi, A., Muñoz-Sabater, J., et al. (2020). The ERA5 global reanalysis. *Quarterly Journal of the Royal Meteorological Society*, *146*(730), 1999–2049. https://doi.org/10.1002/qj.3803

Howard, E., & Washington, R. (2018). Characterizing the synoptic expression of the Angola low. *Journal of Climate*, *31*(17), 7147–7165. https://doi.org/10.1175/JCLI-D-18-0017.1

IRI. (1996). NASA GSFC toms: Total ozone mapping spectrometer [Dataset]. IRI/LDEO Data Library. Retrieved from https://iridl.ldeo.columbia.edu/SOURCES/.NASA/.GSFC/.TOMS/.NIMBUS7/.monthly/.ai/

Jemmett-Smith, B. C., Marsham, J. H., Knippertz, P., & Gilkeson, C. A. (2015). Quantifying global dust devil occurrence from meteorological analyses. *Geophysical Research Letters*, *42*(4), 1275–1282. https://doi.org/10.1002/2015GL063078

Jickells, T. D., An, Z. S., Andersen, K. K., Baker, A. R., Bergametti, G., Brooks, N., et al. (2005). Global iron connections between desert dust, ocean biogeochemistry, and climate. *Science*, *308*(5718), 67–71. https://doi.org/10.1126/science.1105959

Knippertz, P., & Todd, M. C. (2012). Mineral dust aerosols over the Sahara: Meteorological controls on emission and transport and implications for modeling. *Reviews of Geophysics*, *50*(1), RG1007. https://doi.org/10.1029/2011RG000362

Kok, J. F., Parteli, E. J. R., Michaels, T. I., & Karam, D. B. (2012). The physics of wind-blown sand and dust. *Reports on Progress in Physics*, *75*(10), 106901. https://doi.org/10.1088/0034-4885/75/10/106901

Koren, I., Kaufman, Y. J., Washington, R., Todd, M. C., Rudich, Y., Martins, J. V., & Rosenfeld, D. (2006). The Bodélé Depression: A single spot in the Sahara that provides most of the mineral dust to the amazon forest. *Environmental Research Letters*, *1*(1), 014005. https://doi.org/10.1088/1748-9326/1/1/014005

Lindesay, J. A., & Tyson, P. D. (1990). Thermo-topographically induced boundary layer oscillations over the central Namib, southern Africa. *International Journal of Climatology*, *10*(1), 63–77. https://doi.org/10.1002/joc.3370100108

Mahowald, N. M., Baker, A. R., Bergametti, G., Brooks, N., Duce, R. A., Jickells, T. D., et al. (2005). Atmospheric global dust cycle and iron inputs to the ocean. *Global Biogeochemical Cycles*, *19*(4), GB4025. https://doi.org/10.1029/2004GB002402

Mahowald, N. M., Bryant, R. G., del Corral, J., & Steinberger, L. (2003). Ephemeral lakes and desert dust sources. *Geophysical Research Letters*, *30*(2), 1074. https://doi.org/10.1029/2002GL016041

Mahowald, N. M., & Kiehl, L. M. (2003). Mineral aerosol and cloud interactions. *Geophysical Research Letters*, *30*(9), 1475. https://doi.org/10.1029/2002GL016762

Marsham, J. H., Hobby, M., Allen, C. J. T., Banks, J. R., Bart, M., Brooks, B. J., et al. (2013). Meteorology and dust in the central Sahara: Observations from fennec supersite-1 during the June 2011 intensive observation period. *Journal of Geophysical Research: Atmospheres*, *118*(10), 4069–4089. https://doi.org/10.1002/jgrd.50211

McPeters, R. D., Bhartia, P. K., Krueger, A. J., Herman, J. R., Schlesinger, B. M., Wellemeyer, C. G., et al. (1996). *Nimbus–7 total ozone mapping spectrometer (TOMS) data products user's guide*. NASA Reference Publication.

Middleton, N. (2017). Desert dust hazards: A global review. *Aeolian Research*, *24*, 53–63. https://doi.org/10.1016/j.aeolia.2016.12.001

Morcrette, J.-J., Barker, H. W., Cole, J. N. S., Iacono, M. J., & Pincus, R. (2008). Impact of a new radiation package, MCRAD, in the ECMWF integrated forecasting system. *Monthly Weather Review*, *136*(12), 4773–4798. https://doi.org/10.1175/2008MWR2363.1

Munday, C., & Washington, R. (2017). Circulation controls on southern African precipitation in coupled models: The role of the Angola low. *Journal of Geophysical Research: Atmospheres*, *122*(2), 861–877. https://doi.org/10.1002/2016JD025736

Murray, J. E., Brindley, H. E., Bryant, R. G., Russell, J. E., Jenkins, K. F., & Washington, R. (2016). Enhancing weak transient signals in SEVIRI false color imagery: Application to dust source detection in southern Africa. *Journal of Geophysical Research: Atmospheres*, *121*(17), 10199–10219. https://doi.org/10.1002/2016JD025221

Preston-Whyte, R. A., Diab, R. D., & Sokolic, F. (1994). Thermo-topographically induced winds in the boundary layer over the Etosha pan. *South African Geographical Journal*, *76*(2), 59–62. https://doi.org/10.1080/03736245.1994.9713576

Prospero, J. M., Ginoux, P., Torres, O., Nicholson, S. E., & Gill, T. E. (2002). Environmental characterization of global sources of atmospheric soil dust identified with the nimbus 7 total ozone mapping spectrometer (TOMS) absorbing aerosol product. *Reviews of Geophysics*, *40*(1), 2-1–2-31. https://doi.org/10.1029/2000RG000095

Reason, C. (2017). *Climate of southern Africa*. Oxford University Press. https://doi.org/10.1093/acrefore/9780190228620.013.513

Roberts, A. J., Marsham, J. H., Knippertz, P., Parker, D. J., Bart, M., Garcia-Carreras, L., et al. (2017). New Saharan wind observations reveal substantial biases in analysed dust-generating winds. *Atmospheric Science Letters*, *18*(9), 366–372. https://doi.org/10.1002/asl.765

Rouault, M. (2012). Bi-annual intrusion of tropical water in the northern Benguela upwelling. *Geophysical Research Letters*, *39*(12), L12606. https://doi.org/10.1029/2012GL052099

Schepanski, K., Tegen, I., Laurent, B., Heinold, B., & Macke, A. (2007). A new Saharan dust source activation frequency map derived from MSG-SEVIRI IR-channels. *Geophysical Research Letters*, *34*(18), L18803. https://doi.org/10.1029/2007GL030168

Schepanski, K., Tegen, I., Todd, M. C., Heinold, B., Bönisch, G., Laurent, B., & Macke, A. (2009). Meteorological processes forcing Saharan dust emission inferred from MSG-SEVIRI observations of subdaily dust source activation and numerical models. *Journal of Geophysical Research*, *114*(D10), D10201. https://doi.org/10.1029/2008JD010325

Sinha, P., Hobbs, P. V., Yokelson, R. J., Bertschi, I. T., Blake, D. R., Simpson, I. J., et al. (2003). Emissions of trace gases and particles from savanna fires in southern Africa. *Journal of Geophysical Research*, *108*(D13), 8487. https://doi.org/10.1029/2002JD002325

Smith, R. K., & Spengler, T. (2011). The dynamics of heat lows over elevated terrain. *Quarterly Journal of the Royal Meteorological Society*, *137*(654), 250–263. https://doi.org/10.1002/qj.737

Todd, M. C., Washington, R., Raghavan, S., Lizcano, G., & Knippertz, P. (2008). Regional model simulations of the Bodélé low-level jet of northern Chad during the Bodélé dust experiment (bodex 2005). *Journal of Climate*, *21*(5), 995–1012. https://doi.org/10.1175/2007JCLI1766.1

Torres, O., Bhartia, P. K., Herman, J. R., Sinyuk, A., Ginoux, P., & Holben, B. (2002). A long-term record of aerosol optical depth from TOMS observations and comparison to aeronet measurements. *Journal of the Atmospheric Sciences*, *59*(3), 398–413. https://doi.org/10.1175/1520-0469(2002)059⟨0398:ALTROA⟩2.0.CO;2

Venegas, S. A., Mysak, L. A., & Straub, D. N. (1997). Atmosphere–ocean coupled variability in the south Atlantic. *Journal of Climate*, *10*(11), 2904–2920. https://doi.org/10.1175/1520-0442(1997)010⟨2904:AOCVIT⟩2.0.CO;2

Vickery, K. J., & Eckardt, F. D. (2013). Dust emission controls on the lower Kuiseb river valley, central Namib. *Aeolian Research*, *10*, 125–133. https://doi.org/10.1016/j.aeolia.2013.02.006

Vickery, K. J., Eckardt, F. D., & Bryant, R. G. (2013). A sub-basin scale dust plume source frequency inventory for southern Africa, 2005–2008. *Geophysical Research Letters*, *40*(19), 5274–5279. https://doi.org/10.1002/grl.50968

Vizy, E. K., & Cook, K. H. (2016). Understanding long-term (1982–2013) multi-decadal change in the equatorial and subtropical South Atlantic climate. *Climate Dynamics*, *46*(7–8), 2087–2113. https://doi.org/10.1007/s00382-015-2691-1

Wagener, T., Guieu, C., Losno, R., Bonnet, S., & Mahowald, N. (2008). Revisiting atmospheric dust export to the southern hemisphere ocean: Biogeochemical implications. *Global Biogeochemical Cycles*, *22*(2), GB2006. https://doi.org/10.1029/2007GB002984

Washington, R., Todd, M., Middleton, N. J., & Goudie, A. S. (2003). Dust-storm source areas determined by the total ozone monitoring spectrometer and surface observations. *Annals of the Association of American Geographers*, *93*(2), 297–313. https://doi.org/10.1111/1467-8306.9302003

Washington, R., & Todd, M. C. (2005). Atmospheric controls on mineral dust emission from the Bodélé Depression, Chad: The role of the low level jet. *Geophysical Research Letters*, *32*(17), L17701. https://doi.org/10.1029/2005GL023597

Washington, R., Todd, M. C., Engelstaedter, S., Mbainayel, S., & Mitchell, F. (2006). Dust and the low-level circulation over the Bodélé Depression, Chad: Observations from bodex 2005. *Journal of Geophysical Research*, *111*(D3), D03201. https://doi.org/10.1029/2005JD006502

Wiggs, G. F. S., Bullard, J. E., Garvey, B., & Castro, I. (2002). Interactions between airflow and valley topography with implications for Aeolian sediment transport. *Physical Geography*, *23*(5), 366–380. https://doi.org/10.2747/0272-3646.23.5.366

Zunckel, M., Hong, Y., Brassel, K., & O'Beirne, S. (1996). Characteristics of the nocturnal boundary layer: Okaukuejo, Namibia, during safari-92. *Journal of Geophysical Research*, *101*(D19), 23757–23766. https://doi.org/10.1029/95JD00624